J. Fluid Mech. (2000), *vol.* 419, *pp.* 93–124. Printed in the United Kingdom

Stability and bifurcations in stratified Taylor–Couette flow

By F. CATON, B. JANIAUD AND E. J. HOPFINGER

LEGI, CNRS-UJF-INPG, B.P. 53 X, 38041 Grenoble Cedex 9 France

(Received 24 February 1999 and in revised form 13 April 2000)

In this article we present new experimental and theoretical results which were obtained for the flow between two concentric cylinders, with the inner one rotating and in the presence of an axial, stable density stratification. This system is characterized by two control parameters: one destabilizing, the rotation rate of the inner cylinder; and the other stabilizing, the stratification.

Two oscillatory linear stability analyses assuming axisymmetric flow conditions are presented. First an eigenmode linear stability analysis is performed, using the small-gap approximation. The solutions obtained give insight into the instability mechanisms and indicate the existence of a confined internal gravity wave mode at the onset of instability. In the second stability analysis, only diffusion is neglected, predicting accurately the instability threshold as well as the critical pulsation for all the stratifications used in the experiments.

Experiments show that the basic, purely azimuthal flow (circular Couette flow) is destabilized through a supercritical Hopf bifurcation to an oscillatory flow of confined internal gravity waves, in excellent agreement with the linear stability analysis. The secondary bifurcation, which takes the system to a pattern of drifting non-axisymmetric vortices, is a saddle-node bifurcation. The proposed bifurcation diagram shows a global bifurcation, and explains the discrepancies between previous experimental and numerical results. For slightly larger values of the rotation rate, weakly turbulent spectra are obtained, indicating an early appearance of weak turbulence: stationary structures and defects coexist. Moreover, in this regime, there is a large distribution of structure sizes. Visualizations of the next regime exhibit constant-wavelength structures and fluid exchange between neighbouring cells, similar to wavy vortices. Their existence is explained by a simple energy argument.

The generalization of the bifurcation diagram to hydrodynamic systems with one destabilizing and one stabilizing control parameter is discussed. A qualitative argument is derived to discriminate between oscillatory and stationary onset of instability in the general case.

1. Introduction

Since the pioneering works of Couette (1890) and Taylor (1923), over 2000 experimental, numerical and theoretical studies have considered different aspects of circular Couette flow (see e.g. Andereck, Liu & Swinney 1986; Di Prima & Swinney 1981). However, Taylor–Couette flow with axial density stratification has received little attention (Thorpe 1966; Withjack & Chen 1974; Boubnov, Gledzer & Hopfinger 1995; Hua, Le Gentil & Orlandi 1997*a*). The study of this situation is motivated by its possible relation to sub-thermocline equatorial jet formation which might have its

origin in a centrifugal-type instability (Hua, Moore & Le Gentil 1997*b*). Stratified Taylor–Couette flow is also an interesting dynamical system. Indeed, the transition to chaos in extended nonlinear systems is still an open question (Manneville 1991; Guckenheimer & Holmes 1983; Cross & Hohenberg 1993). In particular, in systems with two control parameters, the oscillatory nature of the primary bifurcation is likely to change the scenario (Knobloch 1997; Schöpf & Zimmermann 1993) and is just beginning to be explored (Ashwin & Rucklidge 1998). The question of the selection mechanism of the primary instability (stationary or oscillatory) has been addressed for a long time (Thorpe 1966), but has never received an appropriate answer. As will be shown in this article, a primary Hopf bifurcation can be obtained by adding a stabilizing control parameter, a stable stratification allowing the existence of waves, to the well-known Taylor–Couette flow (Andereck *et al.* 1986), with only the inner cylinder rotating.

In the present paper new experimental and theoretical results for stably stratified circular Couette flow are presented using an improved version of the apparatus of Boubnov *et al.* (1995). These results clarify and complement substantially the recent results reported by Boubnov *et al.* (1995) and Hua *et al.* (1997*a*). Boubnov *et al.* (1995) established an original flow regime diagram in the space of the two control parameters Ω and N, where Ω is the rotation rate of the inner cylinder and the buoyancy frequency $N = \sqrt{-(g/\rho_0)(\partial\rho/\partial z)}$ characterizes the stratification. We discuss briefly this diagram which is reproduced from Boubnov *et al.* (1995) in figure 1.

When $N = 0$, the standard homogeneous Taylor–Couette regimes are recovered, that is the azimuthal Couette flow is destabilized at a critical rotation rate $\Omega_c(N = 0) \simeq 0.2$ rad s^{-1} (for tap water). This gives a critical Reynolds number $Re_c(N = 0) \simeq 90$, in agreement with previous results (Di Prima & Swinney 1981). At $\Omega_c(N = 0)$ stationary vortices of height equal to the gap width (Taylor vortices) appear. For non-zero stratification, new flow regimes are observed. Their succession for fixed N and increasing Ω is the same for all stratifications, when $N > 0.4$ rad s^{-1}, except in the turbulent regimes. For a rotation rate in domain A of the diagram, purely azimuthal Couette flow is obtained. When, for fixed N, the rotation rate of the inner cylinder, Ω, is increased up to a critical value $\Omega_c(N)$, an unstable regime, labelled S for stratified vortex regime, appears. The critical value $\Omega_c(N)$ increases with N, reflecting the stabilizing effect of the stratification. The vortices in this regime are non-axisymmetric and flattened by the stratification, their vertical size being roughly equal to half the gap width. The regime labelled T corresponds to the existence of vortices looking like Taylor vortices. Between these regimes, a transition region denoted by ST exists, where the size of the vortex structures is not well defined. By further increasing Ω, the CT regime (Compact Taylor vortices) appears, where vortices are coupled in pairs.

The study of Hua *et al.* (1997*a*) consists of three-dimensional direct numerical simulations of the Navier–Stokes equations with an additional equation for density. The dimensions of the simulated flow configuration are the same as in the experiments. The simulations exhibit transition values in quantitative agreement with the experiments though there are important qualitative discrepancies for the first regimes. For instance, the onset of the instability is shown in the numerical simulations to be an axisymmetric oscillatory regime, created through a direct Hopf bifurcation. It is also shown that the next transitions are mainly temporal transitions, the azimuthally dependent part of the flow playing only a secondary role. Indeed, the transition values and vertical length scales are very close in two- and three-dimensional simulations. For this reason, we have performed temporal density fluctuation measurements to study the temporal evolution of the density field in the different flow regimes.

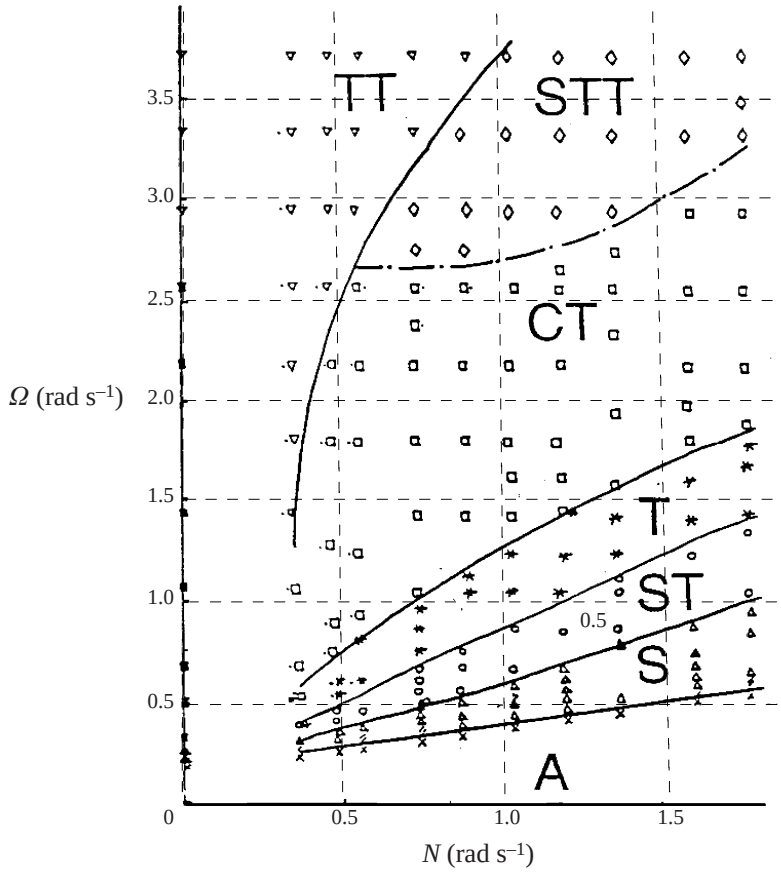

FIGURE 1. Experimental flow regimes and transitions obtained by Boubnov *et al.* (1995). $N = (-(g/\rho_0)(\partial\rho/\partial z))^{1/2}$ is the buoyancy frequency and Ω is the rotation rate of the inner cylinder.

In § 2, the experimental apparatus, techniques and procedures are presented. Section 3 is concerned with the linear stability analyses. The experimental results and interpretation with the bifurcation diagram are presented in § 4. Further discussions and conclusions are presented in § 5.

2. Experimental setup

2.1. *Apparatus*

The stratified Taylor–Couette system used in our experiments is an improved version of the one described in Boubnov *et al.* (1995), and is schematically shown in figure 2. It consists of two precision-machined Plexiglas coaxial cylinders of radii $b = 52 \pm 0.1$ mm and $a = 40 \pm 0.1$ mm, indicating a rather large gap: $\eta = a/b = 0.77$. The length of the cylinders H is 573 mm giving a large aspect ratio, $\Gamma = H/(b-a) = 48$. Moreover, the stratification decouples events in different layers (Billant & Chomaz 2000), so that end effects are of no importance in stratified Taylor–Couette flow. The inner cylinder is rotated by a motor (Crouzet motor, France), between 0 and 110 r.p.m. Its rotation rate Ω is maintained constant within 0.1%. The outer cylinder as well as bottom and top boundaries remain fixed. The cylinders are placed in a square, transparent box filled with water, which helps to keep the system at a constant temperature,

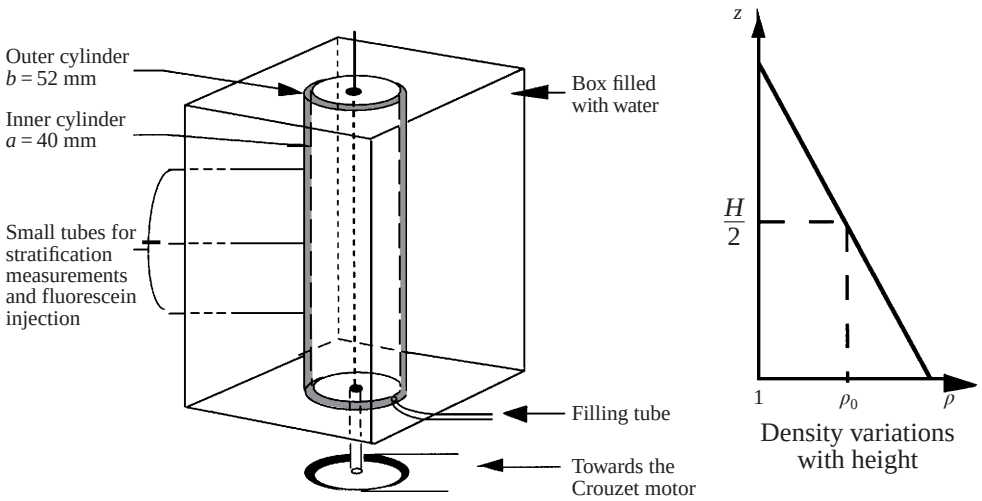

FIGURE 2. Experimental apparatus for the stratified Taylor–Couette flow and imposed stratification.

and reduces optical distortions for visualizations (water has roughly the same optical index as Plexiglas). In the gap between the cylinders, a stable axially linear density stratification is established by a salt solution using the 'double-bucket' filling method (Oster 1965; Caton 1998). The stratification is measured by withdrawing, at three different heights (respectively 90, 228 and 430 mm from the bottom) small samples of fluid and measuring the refractive index. The linearity of the density profile is also checked with shadowgraphs, in which the surface of the inner cylinder appears as a straight line inclined at some angle to the vertical, the inclination being proportional to the buoyancy frequency (N). The deviations from linearity are less than 7% over the whole height. Generally, four values of the stratification were used: $N = 0.68, 0.82, 0.88$ and $0.925\,\mathrm{rad\,s^{-1}}$.

2.2. *Visualizations*

A laser-induced fluorescence technique is used for the visualization of the flow structures. A fluorescent dye solution is injected into the gap through one of the density measurement tubes, the injection being gravity controlled. A laser sheet cutting through the axis of the cylinders excites the fluorescein, and the resulting images are recorded by a high resolution (752 by 582 pixels) CCD Cohu camera linked to a Sony S-VHS video-recorder. Two different injection procedures were used. One, to observe non-overturning structures, is called the 'line' method, which consists in injecting into established flow a fluorescein solution of a density different from that of the fluid at the height of injection. This creates a line of fluorescein which spirals, because of the azimuthal shear, in the gap. In purely azimuthal flow (circular Couette flow), the intersection of this spiral with the laser sheet shows vertical lines the number of which grows in time. The second procedure (the 'patch' method) consists in injecting into established flow a fluorescein dye solution of the same density as the fluid at the injection height. The fluorescein is then advected by the structures.

2.3. *Temporal density fluctuation measurements*

The simplest quantity to measure in our system is the density; velocity measurements are of interest, but are cumbersome (Wereley & Lueptow 1998). For the stratifications

used, the density variations are about 10% over the total height of the cylinders. Over the size of the structures ($\simeq$ 10 mm), these variations should be less than 0.1%. For such small variations, the conductivity and density fluctuations are proportional. Single-point conductivity probes were designed with a signal to noise ratio of over 7 decades and a small temporal drift, which was subtracted from the data. Two such probes were placed flush with the outer cylinder wall (to avoid flow perturbations), at mid-height of the cylinders, and spaced by an azimuthal angle of roughly $\pi/2$. The electric circuit is closed by the earth positioned at the top of the cylinders. The spatial resolution of the probe is of the order of the diameter of the platinum wire (0.125 mm). The temporal resolution ($\simeq$ 10 ms) is much smaller than any time scale of our system ($\simeq$ 10 s).

These probes are linked to a signal acquisition system with sampling rates varying from 1 to 2 Hz and an acquisition time of 30 to 120 mn. The upper time limit is imposed by the mixing time and the need to perform several experiments for one filling of the system. The signal analysis is performed with Matlab software. For more details concerning the experimental techniques and procedures, see Caton (1998).

2.4. *Evolution of the density profile*

The density profile is one of the control parameters. It is, therefore, important to know how long it would take to evolve from a linear to a step-like profile, that is to mix the density within a vortex. In our system, it is not possible to drop a density probe vertically in the gap, but the temporal density fluctuation measurements at one point can be related to the spatial variation. Indeed, the maximum amplitude of the density fluctuations is proportional to the density variations over the height of a vortex and thus decreases when mixing occurs. The amplitude would be close to zero when the density is homogeneously mixed in the structure, that is when the profile is step-like.

During a 5 hour test in the stratified vortex regime (S), the recorded amplitude of the density fluctuations decreased by less than 30%. This shows that mixing is difficult in salt-stratified fluids, as observed in previous studies. For example, in the *turbulent* wake of a cylindrical rod moved back and forth in a stably stratified fluid, less than 5% of the kinetic energy of the rod is used for mixing (Park, Whitehead & Gnanadeskian 1994). For Richardson (Ri) and Reynolds (Re) numbers similar to ours ($Ri \simeq 5$, $Re \simeq 200$), the typical mixing time is about 6 hours. Our experiments were always carried out for times less than 5 hours, then a new filling was prepared. These arguments and observations indicate that, in the stratified vortex regime, the density profile is not step-like, but only slightly perturbed from linearity and the value of the buoyancy frequency practically does not change during an experiment.

3. Linear stability analysis

We present in this section two different axisymmetric, oscillatory linear stability analyses. The first one is intended to give insight into the physical instability mechanisms by means of analytical solutions of the approximated problem. The second one neglects only the diffusion, in order to predict accurately the critical values of the control parameters (Ω, N) and order parameters (frequency and wavelength).

3.1. *Governing equations and basic state*

We consider the governing equations for an incompressible stratified viscous fluid, using the Boussinesq approximation. The fluid motion, mass conservation and density

diffusion equations are

$$\left.\begin{aligned}
\frac{\partial u_r}{\partial t} + (\boldsymbol{u}\cdot\nabla)u_r - \frac{u_\varphi^2}{r} &= -\frac{\partial}{\partial r}\left(\frac{p}{\rho_0}\right) + \nu\left(\Delta u_r - \frac{u_r}{r^2} - \frac{2}{r^2}\frac{\partial u_\varphi}{\partial \varphi}\right),\\
\frac{\partial u_\varphi}{\partial t} + (\boldsymbol{u}\cdot\nabla)u_\varphi + \frac{u_r u_\varphi}{r} &= -\frac{\partial}{r\partial \varphi}\left(\frac{p}{\rho_0}\right) + \nu\left(\Delta u_\varphi - \frac{u_\varphi}{r^2} + \frac{2}{r^2}\frac{\partial u_r}{\partial \varphi}\right),\\
\frac{\partial w}{\partial t} + (\boldsymbol{u}\cdot\nabla)w &= -\frac{\partial}{\partial z}\left(\frac{p}{\rho_0}\right) - g\frac{\rho}{\rho_0} + \nu\Delta w,\\
\nabla\cdot\boldsymbol{u} &= 0,\\
\frac{\partial \rho}{\partial t} + (\boldsymbol{u}\cdot\nabla)\rho &= \kappa\Delta\rho,
\end{aligned}\right\} \tag{3.1}$$

where (u_r, u_φ, w) are the velocity components in the cylindrical coordinates (r, φ, z) respectively, ρ is the fluid density and ρ_0 the reference density. The variation of viscosity with density is taken into account through the reference density (Handbook of Chemistry and Physics 1996). In accordance with the Boussinesq approximation, the variation of viscosity with height is neglected.

The velocity boundary conditions are

$$u_\varphi^0|_{r=a} = \Omega a, \;\; u_\varphi^0|_{r=b} = 0, \tag{3.2}$$

where Ω is the rotation rate of the inner cylinder. The boundary conditions for density are

$$\left.\frac{\partial \rho}{\partial r}\right|_{r=a,b} = 0. \tag{3.3}$$

The basic velocity state verifying all the system symmetries is

$$u_\varphi^0 = Ar + \frac{B}{r}, \quad u_r^0 = 0, \quad w^0 = 0, \quad \frac{\partial}{\partial r}\left(\frac{p^0}{\rho_0}\right) = \frac{(u_\varphi^0)^2}{r} \tag{3.4}$$

and after applying the boundary conditions, we get

$$A = -\Omega\frac{a^2}{b^2 - a^2} = -\Omega\frac{\eta^2}{1-\eta^2}, \quad B = -Ab^2 = \Omega\frac{a^2}{1-\eta^2}, \quad \eta = \frac{a}{b}. \tag{3.5}$$

In the experiments, the basic density state is, *a priori*, a time-dependent state because the initial density gradient is not maintained by the boundary conditions. However, if we consider times smaller than the typical diffusion time over the height of the cylinders H^2/κ (more than one year), this gradient can be considered as constant in time. The Schmidt number S_c =(diffusive time)/(viscous time) = 730 is large in our system. We, therefore, choose as time scale the viscous time, which allows us to write the basic state for the density as time-independent:

$$\rho^0(\boldsymbol{r}) = \rho^0(z) = \rho_0\left(1 - \frac{N^2}{g}z\right), \quad N^2 = -\frac{g}{\rho_0}\frac{\partial \rho^0(z)}{\partial z}, \quad \rho_0 = \rho^0(0). \tag{3.6}$$

This basic state is now perturbed by axisymmetric spatio-temporal periodic disturbances:

$$u_r = 0 + u_r', \quad u_\varphi = u_\varphi^0 + u_\varphi', \quad w = 0 + w', \quad p = p^0 + p', \quad \rho = \rho^0(z) + \rho', \tag{3.7}$$

with

$$(u_r', u_\varphi', w', \rho', p')(r, z, t) = (\tilde{u}_r, \tilde{u}_\varphi, \tilde{w}, \tilde{\rho}, \tilde{p})(r)\,\mathrm{e}^{\mathrm{i}(\omega t + kz)}. \tag{3.8}$$

Substituting these expressions in (3.1), linearizing, using the buoyancy frequency, eliminating $\tilde{p}$, $\tilde{w}$, and $\tilde{\rho}$, and using the following relations between differential operators:

$$\hat{\mathrm{D}}\frac{\partial}{\partial r} = \frac{\partial}{\partial r}\hat{\mathrm{D}}, \quad \frac{\partial}{\partial r}\left(\frac{1}{r}\frac{\partial}{\partial r}r\right) = (\hat{\mathrm{D}} + k^2),$$

we get

$$\left.\begin{aligned} ((\kappa\hat{\mathrm{D}} - \mathrm{i}\omega)(\nu\hat{\mathrm{D}} - \mathrm{i}\omega)\hat{\mathrm{D}} + N^2(\hat{\mathrm{D}} + k^2))(\tilde{u}_r) &= 2k^2(\kappa\hat{\mathrm{D}} - \mathrm{i}\omega)\left(A + \frac{B}{r^2}\right)\tilde{u}_\varphi, \\ (\nu\hat{\mathrm{D}} - \mathrm{i}\omega)\tilde{u}_\varphi &= 2A\tilde{u}_r, \\ \hat{\mathrm{D}} &= \frac{\partial^2}{\partial r^2} + \frac{\partial}{r\partial r} - \frac{1}{r^2} - k^2. \end{aligned}\right\} \tag{3.9}$$

For $\kappa = 0$ equation (4.11) of Boubnov *et al.* (1995) is recovered and for $N = 0$ the standard homogeneous Taylor–Couette instability system is recovered (cf. Chandrasekhar 1961).

3.2. *Eigenmode analysis*

We first non-dimensionalize equations (3.9), in the following way:

$$\begin{aligned} \eta = \frac{a}{b}, \quad \alpha = kd, \quad \sigma = \frac{\omega d^2}{\nu}, \quad S_c = \frac{\nu}{\kappa}, \\ \xi = \frac{r-a}{d}, \quad G = \frac{N^2 d^4}{\nu^2}, \quad T = \frac{4\eta^2\Omega^2 d^4}{(1-\eta^2)\nu^2}, \end{aligned} \tag{3.10}$$

where $d = (b - a)$ is the gap width, S_c is the Schmidt or Prandtl number, G the Grashof number and T the Taylor number.

The small-gap approximation consists of an order-0 expansion of (3.9) in $(1 - \eta)$, which leads to

$$\left.\begin{aligned} ((\mathrm{D} - \alpha^2 - \mathrm{i}S_c\sigma)(\mathrm{D} - \alpha^2 - \mathrm{i}\sigma)(\mathrm{D} - \alpha^2) + S_c G\mathrm{D})\tilde{u_r} &= (\mathrm{D} - \alpha^2 - \mathrm{i}S_c\sigma)(1 - \xi)\tilde{u}_\varphi, \\ (\mathrm{D} - \alpha^2 - \mathrm{i}\sigma)\tilde{u}_\varphi &= -T\alpha^2\tilde{u}_r, \end{aligned}\right\} \tag{3.11}$$

with $\mathrm{D} = \partial^2/\partial\xi^2$ and the boundary conditions

$$\left.\begin{aligned} \tilde{u}_\varphi\big|_{\xi=0,1} = \tilde{u}_r\big|_{\xi=0,1} &= 0, \\ \text{free}: \quad \left.\frac{\partial^2\tilde{u}_r}{\partial\xi^2}\right|_{\xi=0,1} = \mathrm{D}\tilde{u}_r\big|_{\xi=0,1} &= 0, \\ \left.\frac{\partial\tilde{\rho}'}{\partial\xi}\right|_{\xi=0,1} &= 0. \end{aligned}\right\} \tag{3.12}$$

The radial and orthoradial velocities are replaced by their Fourier series

$$\left(\tilde{u}_r = \sum_{m=1}^{\infty} A_m \sin(m\pi\xi) \quad \text{and} \quad \tilde{u}_\varphi = \sum_{n=1}^{\infty} A_n \sin(n\pi\xi)\right)$$

in equation (3.11). Projection of (3.11) on the first mode, i.e. multiplying by $\sin(\pi\xi)$

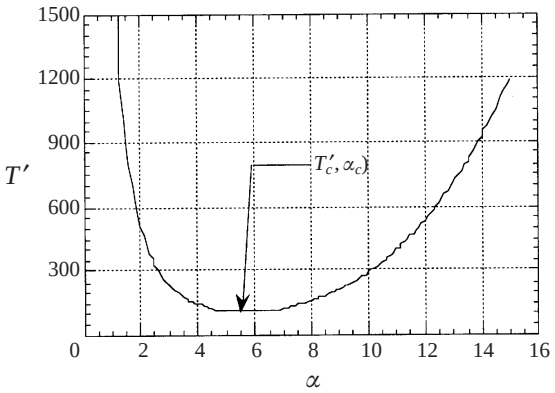

FIGURE 3. Marginal stability curve for $N = 1\,\mathrm{rad\,s^{-1}}$.

and integrating over ξ gives the complex dispersion relation

$$T' = \frac{2}{x(1+x+\mathrm{i}S_c\sigma')}((1+x+\mathrm{i}S_c\sigma')(1+x+\mathrm{i}\sigma')(1+x)+S_cG')(1+x+\mathrm{i}\sigma'), \quad (3.13)$$

where the following changes of variables have been used:

$$x = \frac{\alpha^2}{\pi^2}, \quad \sigma' = \frac{\sigma}{\pi^2}, \quad T' = \frac{T}{\pi^4}, \quad G' = \frac{G}{\pi^4}. \quad (3.14)$$

This dispersion relation is identical within a factor of $\frac{1}{2}$ to the one obtained by Thorpe (1966) for stratified Taylor–Couette flow in the corotating case.

At the onset of instability (marginal stability), the frequency σ is real.

3.2.1. *Oscillatory instability* ($\sigma \neq 0$, *real*)

The Taylor number must be real. So, the imaginary part of (3.13) must be zero, leading to the expression for the frequency of oscillation:

$$\sigma'^2 = -\left(\frac{(1+x)^2}{S_c^2}\right) + \frac{(S_c-1)S_cG'}{2(1+x)S_c^2} \geqslant 0. \quad (3.15)$$

Using (3.15), (3.13) becomes

$$T'^o = \frac{2(S_c+1)^2}{xS_c^2}\left[(1+x)^3 + \frac{S_cG'}{2(S_c+1)}\right], \quad (3.16)$$

where the superscript o stands for oscillatory.

This function is plotted in figure 3 for our experimental geometry, Schmidt number $S_c = 730$ and fixed $N = 1\,\mathrm{rad\,s^{-1}}$.

The minimum of T'^o at x_c^o defines the critical Taylor number and the critical wavenumber:

$$\left.\frac{\partial T'^o}{\partial x}\right|_{x_c^o} = 0 \Rightarrow 2(x_c^o)^3 + 3(x_c^o)^2 = 1 + \frac{S_cG'}{2(S_c+1)}. \quad (3.17)$$

Substituting in (3.16), we get

$$T'^o_c = \frac{6(1+S_c)^2(1+x_c^o)^2}{S_c^2}. \quad (3.18)$$

It is seen that the critical wavenumber and the critical Taylor number depend on

the Schmidt number only through ratios like $(S_c + 1)/S_c$. When S_c is large, it no longer influences the critical wavenumber, the frequency of oscillation or the Taylor number.

3.2.2. *Stationary instability* ($\sigma = 0$)

Equation (3.13) for $\sigma = 0$ gives

$$T'^s = \frac{2}{x}((1+x)^3 + S_c G'), \tag{3.19}$$

where the superscript s stands for stationary. The corresponding expressions for the critical wavenumber and critical Taylor number in the stationary case are

$$2(x_c^s)^3 + 3(x_c^s)^2 = 1 + S_c G' \Rightarrow T'^s_c = 6(1 + x_c^s)^2. \tag{3.20}$$

Now, the critical wavenumber strongly depends on the Schmidt number and hence the critical Taylor number too. As already shown by Thorpe (1966) for the co-rotating stratified Taylor–Couette flow, a critical Schmidt number should exist for which the oscillatory instability switches to a stationary one.

3.2.3. *Selection of the instability character*

The selection criterion between stationary and oscillatory is the respective lower value of the critical Taylor number. Indeed, if $T'^s_c < T'^o_c$, the instability will be stationary and it will be oscillatory if $T'^o_c < T'^s_c$, which depends on the Schmidt number.

For large G' and x, we have

$$x_c^o \sim \left(\frac{S_c G'}{4(S_c+1)}\right)^{1/3}, \quad x_c^s \sim \left(\frac{S_c G'}{2}\right)^{1/3} \tag{3.21}$$

so that $T'^o_c < T'^s_c$ when

$$\frac{(S_c+1)^{2/3}}{S_c} < 2^{1/3}. \tag{3.22}$$

For $G' \gg 1$, the condition for an oscillatory instability is thus $S_c > 1.44$, which is identical to the value obtained by Thorpe (1966) and close to the numerical threshold value $S_c = 1.93$ of Hua *et al.* (1997*a*). A simple physical explanation for a threshold value for the Schmidt number of order 1 can be given. Consider a system with two control parameters, one stabilizing, the other destabilizing. It is widely believed that stationary rolls should be considered as the universal secondary motion resulting from the primary instability (Busse & Clever 1996). This supposes that any effect other than the destabilization can be treated as a perturbation. This will be the case only if the stabilizing parameter disappears faster than the instability appears. In our case, we would have rolls if the typical dissipation time of the stratification d^2/κ were smaller than the instability dissipation time d^2/ν. This yields the criterion $\nu/\kappa = S_c < 1$ for stationary instability.

Another possibility exists to obtain a stationary onset of instability even for large Schmidt numbers. Equation (3.15) shows that σ^2 might be negative, in which case the oscillatory instability would not exist. Solving $\sigma^2 = 0$ with the constraint of equation (3.17) and $S_c = 730$ gives a critical Grashof number $G = 0.9$. This corresponds to a stratification of $N = 10^{-3}\,\mathrm{rad\,s^{-1}}$ which is far below the experimental values used.

In conclusion, the onset of instability should be oscillatory in the experiments, where the Schmidt number is equal to 730, and the buoyancy frequency N larger than $0.1\,\mathrm{rad\,s^{-1}}$.

3.2.4. *Instability mechanisms and scaling laws*

For large Schmidt number, (3.15) to (3.18) reduce to

$$2(x_c^o)^3 + 3(x_c^o)^2 = 1 + \frac{G'}{2}, \tag{3.23a}$$

$$T_c'^o = 6(1 + x_c^o)^2, \tag{3.23b}$$

$$\sigma'^2 = \frac{G'}{2(1+x)}. \tag{3.23c}$$

Writing (3.23*c*) in dimensional variables we get

$$\omega^2 = \frac{N^2}{2(1 + k^2 d^2/\pi^2)} \tag{3.24}$$

This is, except for the 1/2 factor, the dispersion relation for internal gravity waves confined between two vertical planes (Nicolaou, Liu & Stevenson 1993).

Suppose now that $G' \gg 1$. Equation (3.23*a*), in dimensional form, gives

$$x_c^o \sim \left(\frac{G'}{4}\right)^{1/3} \Rightarrow \frac{\lambda_c^o}{2d} = \left(\frac{2\nu\pi^2}{Nd^2}\right)^{1/3}. \tag{3.25}$$

The viscosity plays its usual role, acting like a low-pass filter for the wavenumber. The effect of stratification is the reverse, acting like a high-pass filter. The balance between both effects fixes the wavenumber, which imposes the frequency of the waves through the dispersion relation of confined internal gravity waves.

We want to know whether these mechanisms remain valid somewhat above the onset of instability. For this we derive relations between the parameters at the onset of instability. From (3.23*a*, *b*), the size of the structures at threshold ($\lambda_c^o/2$) can be related to the critical Froude number $Fr_c^o = \Omega_c^o/N$:

$$\frac{\lambda_c^o}{2d} \sim C Fr_c^o, \quad C = \sqrt{\frac{8\eta^2}{3(1-\eta^2)}} = 1.96. \tag{3.26}$$

The frequency of the waves is obtained by substituting (3.23*a*) and equation (3.26) in (3.23*c*):

$$\sigma = \frac{\sqrt{2}}{C^2 (Fr_c^o)^2} = \frac{\sqrt{2}}{C^2} Ri, \tag{3.27}$$

where *Ri* is the Richardson number.

Since these relations are scaling laws, we suppose that they are valid in the whole oscillatory regime. We then obtain the change in flow behaviour in the first unstable regime, for fixed stratification:

$$\delta\lambda = \delta\Omega, \quad \delta\omega = -2\delta\Omega, \tag{3.28}$$

where

$$\delta\omega = \frac{\omega}{\omega_c^o} - 1, \quad \delta\lambda = \frac{\lambda}{\lambda_c^o} - 1, \quad \delta\Omega = \frac{\Omega}{\Omega_c^o} - 1. \tag{3.29}$$

This indicates that, in the first unstable regime, the size of the structure should grow linearly with the control parameter, while the frequency of the waves should *decrease* linearly.

3.3. *Wide-gap analysis*

Here we present the second linear stability analysis which aims at predicting the values of the critical control and order parameters, for the experimental conditions. The perturbations are still axisymmetric and oscillatory. The calculations are performed without the small-gap approximation, with rigid velocity boundary conditions but for an infinite Schmidt number. This means that we only neglect the molecular diffusion, which is reasonable since in the experiments $S_c = 730$. We will follow closely Chandrasekhar's method, the stationary case being here generalized to the oscillatory one.

First, equations (3.9) are non-dimensionalized without the small-gap approximation, taking into account the curvature of the system. The relations between the new non-dimensional parameters (with primes) and the previous one are

$$T' = T\frac{\eta^2}{(1-\eta)^4(1-\eta^2)}, \quad G' = \frac{G}{(1-\eta)^4}, \quad \alpha' = \frac{\alpha}{1-\eta}, \quad \sigma' = \frac{\sigma}{(1-\eta)^2}, \quad r' = \frac{r}{b}. \tag{3.30}$$

Nearly the same equations as (3.11) are obtained, the difference lying in the differential operators. For the following, primes are dropped:

$$\left.\begin{aligned}\left((\mathrm{DD}^* - \alpha^2 - \mathrm{i}\sigma)(\mathrm{DD}^* - \alpha^2) + \mathrm{i}\frac{G}{\sigma}\mathrm{DD}^*\right)\tilde{u}_r = -T\alpha^2\left(\frac{1}{r^2} - 1\right)\tilde{u}_\varphi,\\ (\mathrm{DD}^* - \alpha^2 - \mathrm{i}\sigma)\tilde{u}_\varphi = \tilde{u}_r,\end{aligned}\right\} \tag{3.31}$$

$$\mathrm{D} = \frac{\mathrm{d}}{\mathrm{d}r}, \quad \mathrm{D}^* = \frac{\mathrm{d}}{\mathrm{d}r} + \frac{1}{r}, \tag{3.32}$$

with the rigid velocity boundary conditions at $r = 1$ and $r = \eta$:

$$\tilde{u}_r = \tilde{u}_\phi = \tilde{w} = 0. \tag{3.33}$$

After calculations (cf. Chandrasekhar 1961), the following matricial secular equation is obtained:

$$\det\left|(\alpha_j^4 + \alpha^4 + \mathrm{i}\alpha^2\sigma)N_j\delta_{jk} + \alpha_j^2\left(2\alpha^2 + \mathrm{i}\sigma\left(1 - \frac{G}{\sigma^2}\right)\right)\Delta_{jk}^1 - T\alpha^2\left(p_j\Delta I(\tilde{\alpha}r) + q_j\Delta K(\tilde{\alpha}r) + \frac{\tilde{\alpha}^2(N_j\delta_{jk} - M_{jk}) - \alpha_j^2\mathrm{D}\Delta_{jk}}{\alpha_j^4 - \tilde{\alpha}^4}\right)\right| = 0. \tag{3.34}$$

The α_j are the solutions of the transcendental equation:

$$(\mathrm{DD}^*)^2 y = \left(\frac{\mathrm{d}^2}{\mathrm{d}r^2} + \frac{1}{r}\frac{\mathrm{d}}{\mathrm{d}r} - \frac{1}{r^2}\right)^2 y = \alpha_j^4 y, \tag{3.35}$$

the functions y obeying: $y\big|_{r=1,\eta} = (\mathrm{d}y/\mathrm{d}r)\big|_{r=1,\eta} = 0$

The eigenvectors y of this system can be written as a sum of Bessel functions:

$$C_1(\alpha_j r) = A_j J_1(\alpha_j r) + B_j Y_1(\alpha_j r) + C_j I_1(\alpha_j r) + D_j K_1(\alpha_j r). \tag{3.36}$$

The A_j, B_j, C_j and D_j are determined up to an arbitrary multiplicative constant.

$$\left.\begin{aligned}
N_j &= \int_\eta^1 (u_j(r)+v_j(r))^2\, r\,\mathrm{d}r,\\
\Delta_{jk}^{(\pm1)} &= \int_\eta^1 (u_j(r)-v_j(r))(u_k(r)+v_k(r))r^{(\pm1)}\,\mathrm{d}r,\\
\mathrm{D}\Delta_{jk} &= \Delta_{jk}^{(1)} - \Delta_{jk}^{(-1)},\\
\Delta I_k(\alpha) &= \int_\eta^1 I_k(\alpha)(u_k(r)+v_k(r))\left(r-\frac{1}{r}\right)\,\mathrm{d}r,\\
\Delta K_k(\alpha) &= \int_\eta^1 K_k(\alpha)(u_k(r)+v_k(r))\left(r-\frac{1}{r}\right)\,\mathrm{d}r,\\
M_{jk} &= \int_\eta^1 (u_j(r)+v_j(r))(u_k(r)+v_k(r))\frac{1}{r}\,\mathrm{d}r,\\
u_j(r) &= A_jJ_1(\alpha_jr)+B_jY_1(\alpha_jr),\\
v_j(r) &= C_jI_1(\alpha_jr)+D_jK_1(\alpha_jr),\\
\tilde{\alpha} &= \alpha^2+\mathrm{i}\sigma,\\
p_j &= 2\alpha_j^2/[\Delta(\alpha_j^4-\tilde{\alpha}^4)](u_j(1)K_1(\tilde{\alpha}\eta)-u_j(\eta)K_1(\tilde{\alpha})),\\
q_j &= 2\alpha_j^2/[\Delta(\alpha_j^4-\tilde{\alpha}^4)](u_j(\eta)I_1(\tilde{\alpha})-u_j(1)I_1(\tilde{\alpha})).
\end{aligned}\right\} \tag{3.37}$$

Most integrals have no analytical solutions. The full system has been solved numerically, with two physical constraints: the Taylor number must be real and its derivative with respect to α must be zero. The first result of these calculations is that the frequency of oscillation at the onset is never zero except when there is no stratification. The onset of instability in the experimental situation must, therefore, be oscillatory. The theoretical values will be compared with experimental ones in the next section, which contains the experimental results.

4. Experimental results

4.1. *First unstable regime: the wave regime*

4.1.1. *Visualizations*

The numerical simulations of Hua *et al.* (1997*a*) indicate that the first bifurcation from purely azimuthal Couette flow is a direct Hopf bifurcation leading to a flow regime of 'oscillatory convective modes'. We present in figure 4 dye visualizations of this regime, obtained with the 'line' method.

The pattern has been captured for constant time-steps in one vertical section of the gap. The initially vertical lines of dye are deformed by spatially-periodic oscillations, their wavelength being nearly equal to the gap width ($\lambda \simeq d$). In contrast to the homogeneous case, for which the first unstable regime is stationary (Taylor vortices), the first unstable regime for the stratified case is time dependent. As underlined by previous studies (Boubnov *et al.* 1995; Hua *et al.* 1997*a*), the reduction in vertical wavelength compared with the homogeneous case ($\lambda \simeq 2d$) is directly related to the

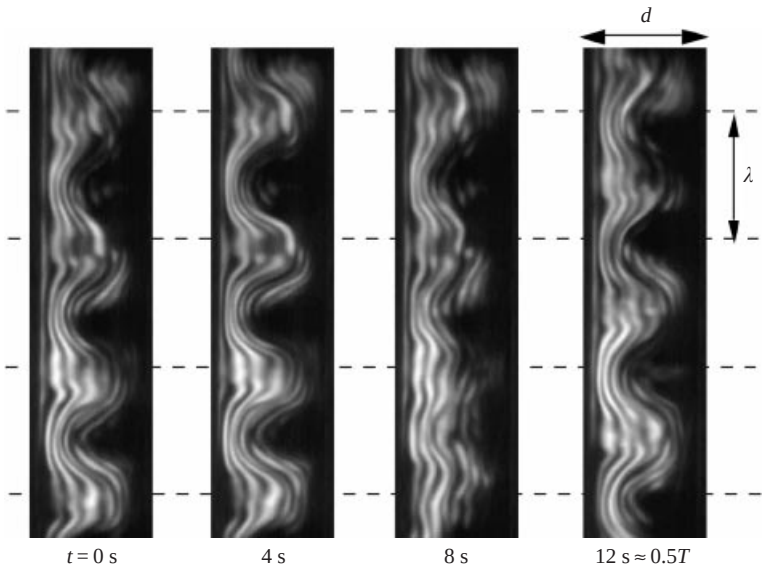

FIGURE 4. Temporal sequence of dye visualizations for $N = 0.88\,\mathrm{rad\,s^{-1}}$, $\Omega = 1.1\ \Omega_c$: standing wave regime.

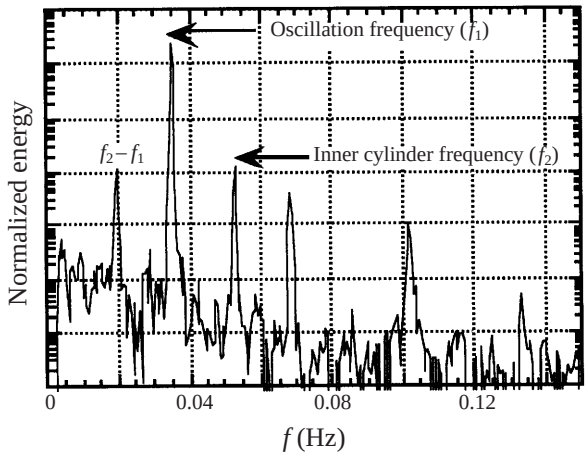

FIGURE 5. Spectral energy of the density fluctuations versus frequency in the wave regime. $N = 0.82\,\mathrm{rad\,s^{-1}}$, $\Omega = 1.03\ \Omega_c$. The oscillation frequency is the wave frequency.

inhibition of vertical motion by stratification. Time-records of this pattern clearly show *oscillations*, the positions of the maxima and minima of oscillation being at rest. No overturning is observed in this regime, indicating *standing waves*.

4.1.2. *Density fluctuation measurements*

The characteristics of the onset of instability have been investigated by measurements of the temporal evolution of the density fluctuations using the conductivity probes described in § 2. For a fixed stratification, when the rotation rate of the inner cylinder is increased up to the critical value Ω_c, the frequency of the waves appears in the power spectra, indicating a Hopf bifurcation. A spectrum obtained in this regime is shown in figure 5.

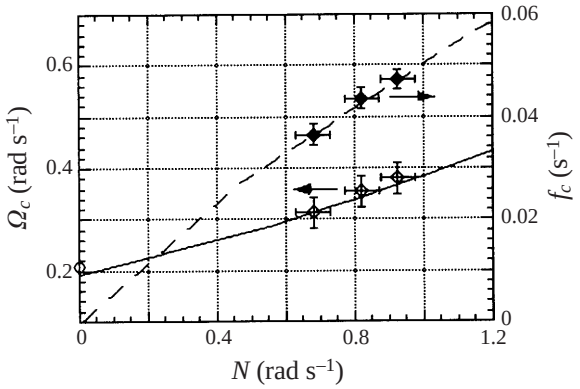

FIGURE 6. Evolution of the critical rotation rate (Ω_c, left axis) and frequency (f_c, right axis) versus stratification: ○, experimental Ω_c and solid line theoretical Ω_c; ●, experimental f_c and dashed line theoretical f_c.

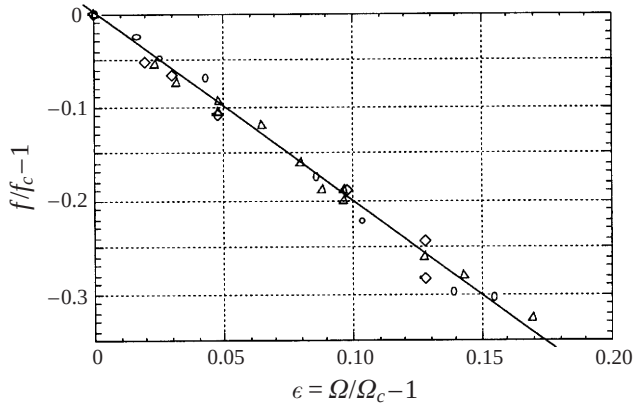

FIGURE 7. Evolution of the non-dimensional frequency deviation from the critical value versus ϵ. ◇, $N = 0.68\,\mathrm{rad\,s^{-1}}$; ○, $N = 0.82\,\mathrm{rad\,s^{-1}}$ and △, $N = 0.925\,\mathrm{rad\,s^{-1}}$. Confined internal waves model from equation (3.28): slope (−2) straight line.

The frequency f_2, corresponding to the rotation rate of the inner cylinder, is present in the spectrum, due to the small circularity defects of the cylinder. Note that the energy contained in this excitation frequency is at least 100 times weaker than the energy contained in the wave frequency.

We first checked that the frequency obtained in the spectra only depends on the rotation rate and the stratification and not on the experimental procedure. There is no hysteresis for the transition between purely azimuthal flow and the wave regime, i.e. the primary bifurcation is a supercritical Hopf bifurcation, which agrees with the numerical simulations of Hua *et al.* (1997*a*). The experimental critical rotation rate (Ω_c) and critical frequency (f_c) for different stratifications are compared in figure 6 with the wide-gap linear stability analysis.

It is seen that agreement between experiments and theory is excellent. The stabilizing effect of stratification is demonstrated by the increase of Ω_c with stratification.

We studied the evolution of the non-dimensional frequency deviation from the critical value ($f/f_c - 1$) in the standing-wave regime as a function of the control parameter ($\epsilon = \Omega/\Omega_c - 1$) for different stratifications (figure 7).

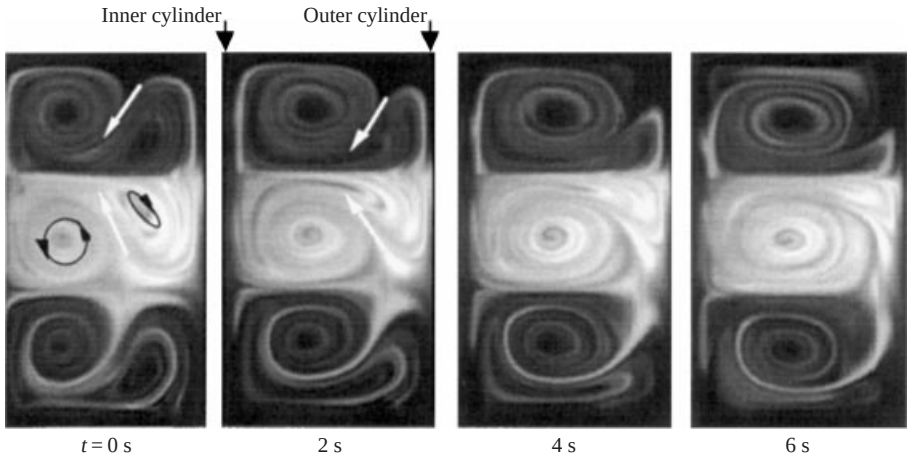

FIGURE 8. Temporal sequence of dye visualizations in the stratified vortex regime, $N = 0.88\,\mathrm{rad\,s^{-1}}$, $\Omega = 1.35\,\Omega_c$. The black arrows indicate the direction of rotation in each vortex and the white arrows, the direction of motion of the boundary between two counter-rotating vortices.

All values collapse remarkably well on a -2 slope straight line which corresponds to the prediction of equations (3.29) and (3.28). Cross-correlated spectra from two probes also show that these waves are *axisymmetric*, the phase shift for the wave frequency being equal to zero. These observations demonstrate that the system bifurcates from the purely azimuthal flow through a supercritical Hopf bifurcation to a state of standing, axisymmetric, confined internal gravity waves.

4.2. *The stratified vortex regime*

4.2.1. *Visualizations*

By further increasing Ω above Ω_c, the second unstable regime appears as a vortex regime (figure 8). The spatio-temporal structure of this regime has also been determined with the fluorescein dye technique, using the 'patch' method.

Overturning is depicted by the presence of small spirals in the structures. As in the wave regime, the vertical size of the structures is compressed by the stratification. Two counter-rotating vortices are present at a given height, and the boundary between two vortices (indicated by the white arrow) appears in the visualization plane at roughly half the rotation rate of the inner cylinder. An image of the structures in the two diametrically opposite plane sections of the gap is shown in figure 9. In this figure, at a given height, the direction of motion of the boundary between two counter-rotating vortices (indicated by the white arrow) is not symmetric with respect to the rotation axis, which indicates that the flow is no longer axisymmetric.

In figure 10 we present a schematic top view of a model of the flow for an azimuthal mode $m = 1$ and its correspondence with the visualizations. The visualizations and this model are in good agreement with the numerical simulations of Hua *et al.* (1997*a*) and the visualizations of Boubnov *et al.* (1995) and Withjack & Chen (1974).

4.2.2. *Density fluctuation measurements*

A temporal signal of the density fluctuations in this stratified vortex regime is presented in figure 11. The signal is clearly periodic, the amplitude of the oscillation being constant over the whole record. This shows that mixing is negligible and the

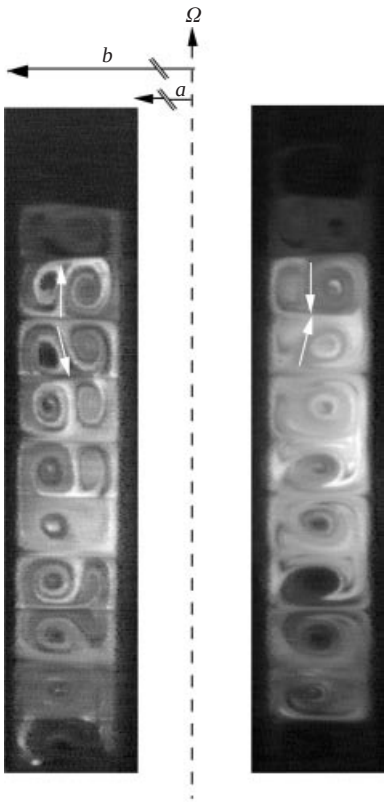

FIGURE 9. Visualization in the stratified vortices in diametrically opposite sections of the gap. The white arrows indicate the direction of motion of the boundary between two counter-rotating vortices. $N = 0.88\,\mathrm{rad\,s^{-1}}$, $\Omega = 1.35\,\Omega_c$.

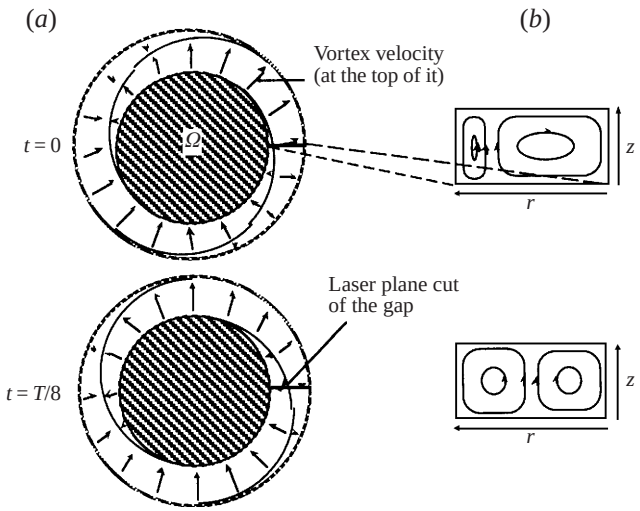

FIGURE 10. Schematic (*a*) top view and (*b*) section of two counter-rotating vortices in the stratified vortex regime (mode $m = 1$).

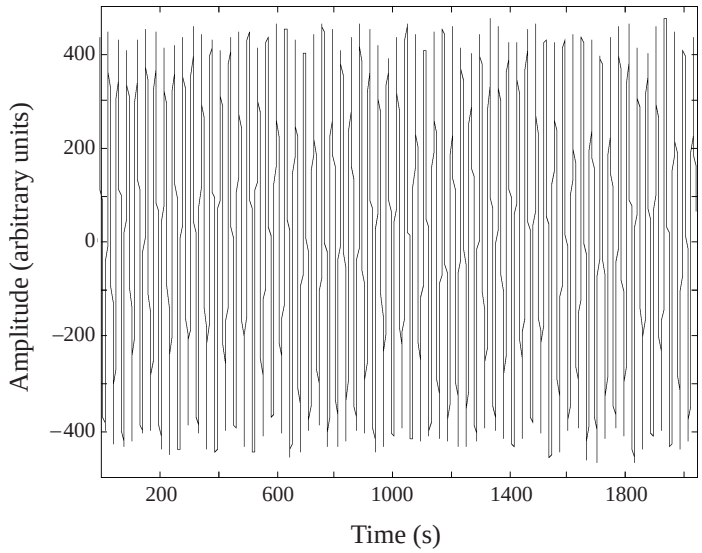

FIGURE 11. Temporal evolution of the density fluctuations in the stratified vortex regime. $N = 0.925\,\mathrm{rad\,s^{-1}}$, $\Omega = 1.17\,\Omega_c$.

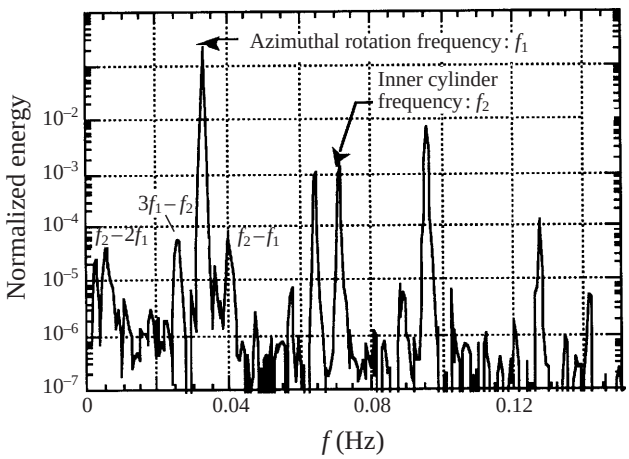

FIGURE 12. Spectral energy of the density fluctuations versus frequency in the stratified vortex regime. The azimuthal rotation frequency corresponds to the frequency of appearance of the boundary between counter-rotating vortices. $N = 0.925\,\mathrm{rad\,s^{-1}}$, $\Omega = 1.17\,\Omega_c$.

basic density profile is only weakly perturbed by the flow, in agreement with the numerical simulations of Hua *et al.* (1997*a*) (their figure 5*a*).

A typical power spectrum of this regime is displayed in figure 12. The inner-cylinder frequency is still present. The main frequency corresponds to the frequency of appearance, in the laboratory frame, of the boundary between the counter-rotating vortices at the same height, that is to the azimuthal rotation frequency of the whole vortex pattern.

The phase shift between the conductivity probes for the fundamental frequency is equal to the angle difference ($\pi/2$) between the probe locations, confirming the

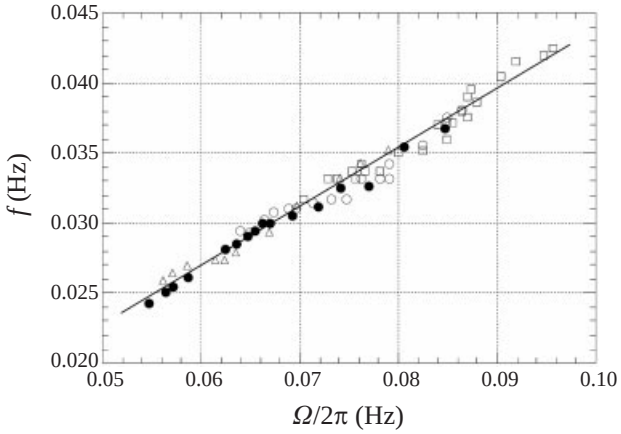

FIGURE 13. Evolution of the azimuthal rotation frequency with the inner cylinder frequency. △, $N = 0.68\,\mathrm{rad\,s^{-1}}$, ○ and ●, $N = 0.82\,\mathrm{rad\,s^{-1}}$, □, $N = 0.925\,\mathrm{rad\,s^{-1}}$. The straight line is a linear fit: $f = 0.0027 + 0.413\Omega/2\pi$, regression coefficient $R = 0.985$.

non-axisymmetry of the flow in this regime. Figure 13 shows that the evolution of this frequency with rotation rate no longer depends on stratification.

The straight line fit in figure 13 verifies the relation

$$f = C^{\mathrm{st}}(m) + m\frac{\langle\Omega^0\rangle}{2\pi} = 0.0027 + \frac{\langle\Omega^0\rangle}{2\pi} \tag{4.1}$$

with

$$\langle\Omega^0\rangle = \frac{\displaystyle\int_a^b (A + B/r^2) r\,\mathrm{d}r}{\displaystyle\int_a^b r\,\mathrm{d}r} = \left(-\frac{a^2}{b^2 - a^2} + \frac{2a^2b^2}{(b^2 - a^2)^2}\ln\frac{b}{a}\right)\Omega = 0.413\,\Omega \tag{4.2}$$

for our apparatus. Here, $m = 1$ is the azimuthal mode and $\langle\Omega^0\rangle$ is the angular velocity calculated for purely azimuthal circular Couette flow, averaged over the volume. In a first approximation, the whole 3D pattern is drifting at this mean angular velocity $\langle\Omega^0\rangle$. Because of the system's azimuthal rotation symmetry (SO2), the non-axisymmetric vortex pattern cannot drift at exactly the mean angular velocity (Knobloch 1997). Hence, the small value at the origin ($C^{\mathrm{st}}(m)$) is the precession frequency, relative to the mean angular velocity. So, the frequency measures the drift velocity of the pattern, i.e. the revolution period of a vortex around the axis of the cylinders. Since there is no other frequency associated with the flow in the spectrum shown in figure 12, the density field is stationary in the frame rotating at the drift velocity of the pattern. Consequently, the vortices are steady in this rotating frame.

4.3. *The wave–vortex transition*

4.3.1. *Observation of hysteresis*

Special attention has been given to the transition between the wave regime and the vortex regime. This transition does *not* correspond to the appearance or disappearance of any frequency in the spectra, nor to a jump in the measured frequency. The transition occurs when the frequency of the waves equals the mean angular velocity.

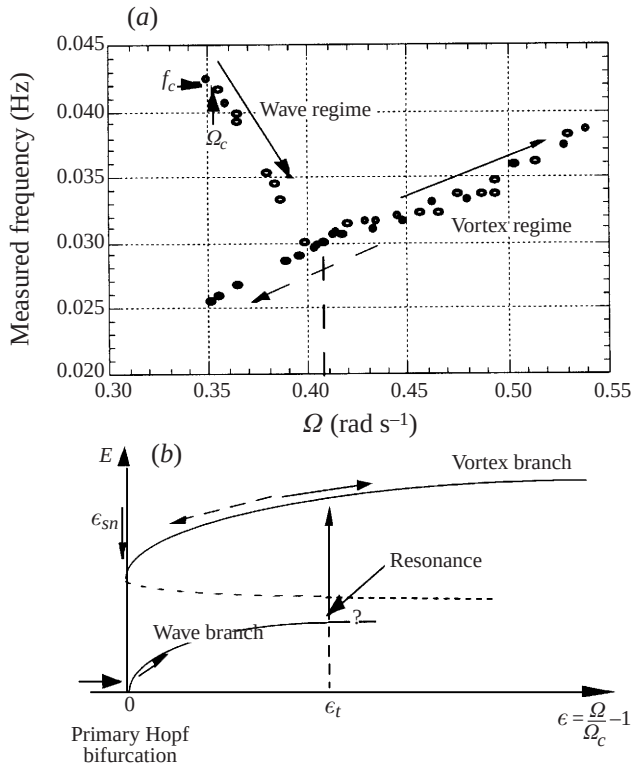

FIGURE 14. (*a*) Hysteresis in the evolution of the measured frequency with the control parameter. ○, increasing; ●, decreasing procedure for $N = 0.82\,\mathrm{rad\,s^{-1}}$. (*b*) Schematic representation of the bifurcation diagram from purely azimuthal flow to vortices. The ordinate is the energy E of the perturbations relative to the basic state.

The only hint of a transition in the spectra is that for cross-correlated spectra from two probes, the phase shift for the measured frequency is zero in the wave regime and equal to $\pi/2$ in the vortex regime. The evolution of the main frequency versus the rotation rate, when increasing or decreasing the control parameter by small steps, is plotted in figure 14(*a*). At Ω_t, when increasing the control parameter, the variation of the frequency with the control parameter changes radically, indicating the transition from the wave to the vortex regimes.

These measurements show that the frequency can have two different values for one rotation rate, depending on the procedure (increasing or decreasing). This hysteresis implies that the bifurcation between the wave regime and the vortex regime is *a subcritical bifurcation*, namely that the vortex branch is created through a saddle-node bifurcation. As explained in § 2.4, the basic density profile is only slightly perturbed from linearity in the stratified vortex regime, so the hysteresis is not due to mixing. Let us recall that only one frequency is present in the wave regime (oscillation) and in the vortex regime (azimuthal rotation) and these frequencies have different physical origins. Indeed in the reference frame rotating at the drift velocity of the pattern, the flow is *stationary* in the stratified vortex regime, whereas in the wave regime the flow is still oscillatory. So, it is not likely that these solutions connect in the phase space. This suggest that the saddle-node bifurcation is a *global bifurcation.*

4.3.2. *Bifurcation diagram*

From these observations a plausible schematic projection in the plane (ϵ, E) (where E is a typical energy of a mode) of the diagram of bifurcations is proposed in figure 14(b). Our experimental procedure did not allow us to measure the energy of the mode, so E is only a qualitative estimation. The true dimension of the diagram is six: each mode energy and frequency, ϵ and N. Figure 14(a) is its projection in a (ϵ, frequency)-plane. For fixed stratification, this bifurcation diagram can be described as follows. A branch of waves is created through a direct Hopf bifurcation at the abscissa $\epsilon_c = 0$ (by definition). The stable and unstable branches of stratified vortices appear in a saddle-node bifurcation at ϵ_{sn}. At ϵ_t the system jumps onto the stable branch of the vortices. Decreasing ϵ from the drifting vortices branch, the system will follow this branch until $\epsilon = \epsilon_{sn}$. Then it can jump either onto the purely azimuthal flow if $\epsilon_{sn} < 0$, or onto the wave branch if $\epsilon_{sn} > 0$. In our system, ϵ_{sn} is slightly negative. Experimentally we do not know what happens to the oscillatory branch after the transition point ϵ_t.

4.3.3. *A possible mechanism for the wave–vortex transition*

The transition from the wave to the stratified vortex regimes takes place when the frequency of the waves equals the mean angular velocity of the bulk of the azimuthal flow. We propose here a simple qualitative argument which might explain this transition. First recall that in the wave regime, the azimuthal velocity contains a temporally periodic perturbation. From equations (3.7) and (3.8), ignoring the axial periodicity, the local angular velocity is

$$\frac{u_\varphi(r)}{r} = \Omega^0(r) + A_\varphi(r)\cos\omega t. \tag{4.3}$$

So the waves modulate the angular velocity of the bulk of the fluid at their own frequency. As seen in the non-axisymmetric vortex regime (§ 4.2), the system can be interpreted as a system rotating at the averaged angular velocity. In the wave regime, this averaged angular velocity can be written as

$$\langle\Omega\rangle = \langle\Omega^0\rangle(1 + \alpha\cos\omega t), \tag{4.4}$$

where α is the forcing amplitude, related to the amplitude of the waves A_φ. When the wave frequency ω equals the mean rotation frequency $\langle\Omega^0\rangle$, we believe that a parametric resonance might occur. This resonance would increase the velocity fluctuations and thus allow the system to explore the phase space. So it can leave the wave attractor and fall onto the vortices attractor.

4.3.4. *Implications of the bifurcation diagram*

The bifurcation diagram explains the differences between the present results and those of Boubnov *et al.* (1995). The onset of instability reported by Boubnov *et al.* is a non-axisymmetric flow regime with vortices, called S in figure 1. The experimental apparatus of Boubnov *et al.* had circularity defects of about 1 mm for a gap width of 12 mm.

We performed density fluctuation measurements in the apparatus used by Boubnov *et al.* (1995) for which a typical spectrum is plotted in figure 15. The main point is that the excitation frequency energy is now 100 times larger than the energy related to the vortices azimuthal rotation frequency (compare with figure 12). This large noise amplitude forces the system to jump directly onto the drifting vortices branch, whenever possible. Since in these experiments non-axisymmetric vortices were always

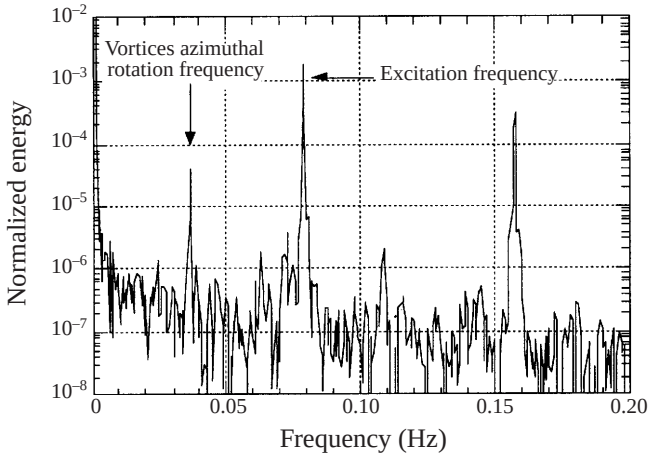

FIGURE 15. Spectral energy of density fluctuations in the vortex regime, obtained on Boubnov *et al.*'s experimental system.

obtained at the onset of instability, the abscissa of the saddle-node bifurcation ϵ_{sn} was measured instead of the real onset of instability. Comparison of these values with the theoretical and numerical critical values shows that ϵ_{sn} is close to zero for all the stratifications. Why this is the case remains unexplained.

Up to this point, we have not mentioned the influence of varying the stratification on the bifurcation diagram. It should modify the abscissa of the transition and saddle-node bifurcation points. At the transition point, according to the experimental curve (see figure 14*a*), the wave frequency and the angular drift velocity of the vortices are equal. Hence, knowing the theoretical evolution of the wave frequency ω from equation (3.28):

$$\omega(N) = [1 - 2\epsilon]\omega_c(N), \tag{4.5}$$

and the angular drift velocity of the vortex pattern ω_{azi} from equation (4.1):

$$\omega_{azi} = 0.413[\epsilon + 1]\Omega_c(N) + 2\pi \times 0.0027, \tag{4.6}$$

as a function of ϵ and N, the transition point can be predicted as a function of the stratification. In view of the equality of these pulsations at the transition point, one gets

$$\epsilon_t(N) = \frac{\omega_c(N) - [2\pi \times 0.0027 + 0.413\,\Omega_c(N)]}{0.413\,\Omega_c(N) + 2\,\omega_c(N)}. \tag{4.7}$$

In figure 16 are plotted the theoretical (equation (4.7)), experimental and numerical (simulations of Hua *et al.* 1997*a*) values of ϵ_t as a function of stratification. The agreement between experimental, numerical and theoretical values of the transition point is excellent.

4.4. *The T regime*

4.4.1. *Visualizations*

The next regimes observed by Boubnov *et al.* (1995) are the T and ST regimes (figure 1). According to their observations, the T regime corresponds to the presence of structures looking like Taylor vortices, the ST regime being a transition regime.

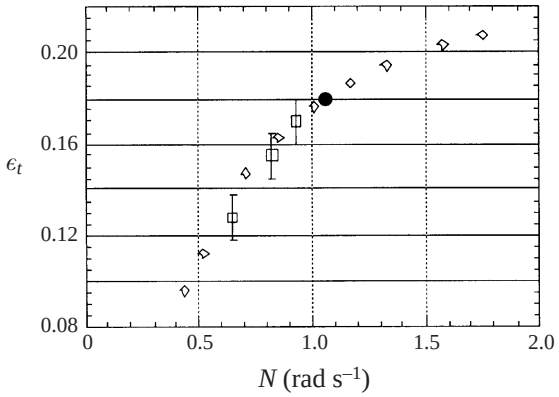

FIGURE 16. Transition value ϵ_t versus stratification. ◇, Theory; □, experiments; ●, simulation.

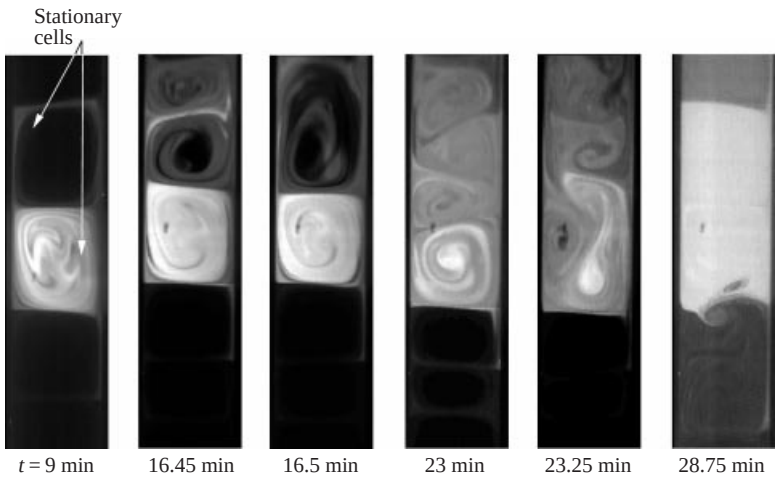

FIGURE 17. Patch visualizations of the T regime $N = 0.88\,\mathrm{rad\,s^{-1}}$, $\Omega = 2.5\,\Omega_c$.

Our observations indicates that there is no qualitative difference between these two regimes. The whole regime will now be called T.

In figure 17 'patch' visualizations exhibit the main feature of this regime. In the first snapshot ($t = 9$ min) two stationary vortices of aspect ratio slightly larger than one, looking like Taylor vortices, are observed. These are replaced at $t = 16.45$ min by more complex structures. At $t = 23$ min turbulent-like structures, called defects, are clearly present. This twofold behaviour (stationary structures and defects) of the flow exists in the whole parameter range of the T regime.

4.4.2. *Density measurements*

Temporal density fluctuations measurements were also performed in the established flow regime. Such a record is shown in figure 18. The signal is strongly non-stationary with a large variation of the mean value. The amplitude of the fluctuations also varies widely, without any clear trend.

A typical spectrum of the density fluctuations is presented in figure 19 (light line). In order to emphasize the spectral peaks, a mean spectral energy density (thick line) is also calculated, by dividing the whole signal into 8 windows of 512 points. The

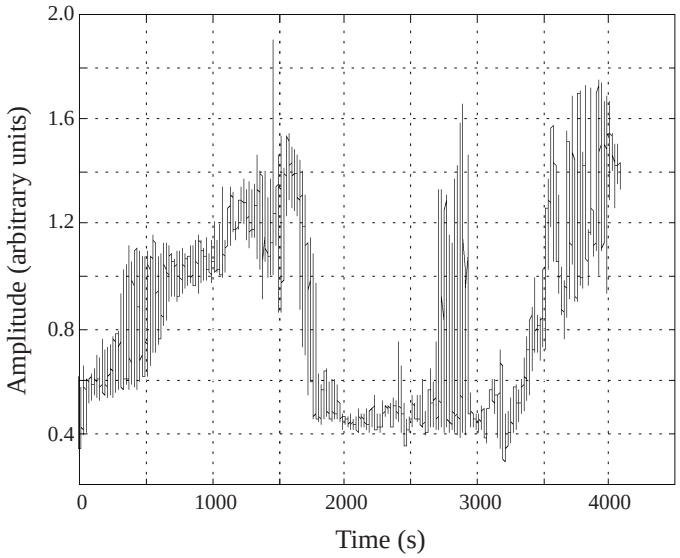

FIGURE 18. Temporal evolution of the density fluctuations. $N = 0.82\,\mathrm{rad\,s^{-1}}$, $\Omega = 2\,\Omega_c$.

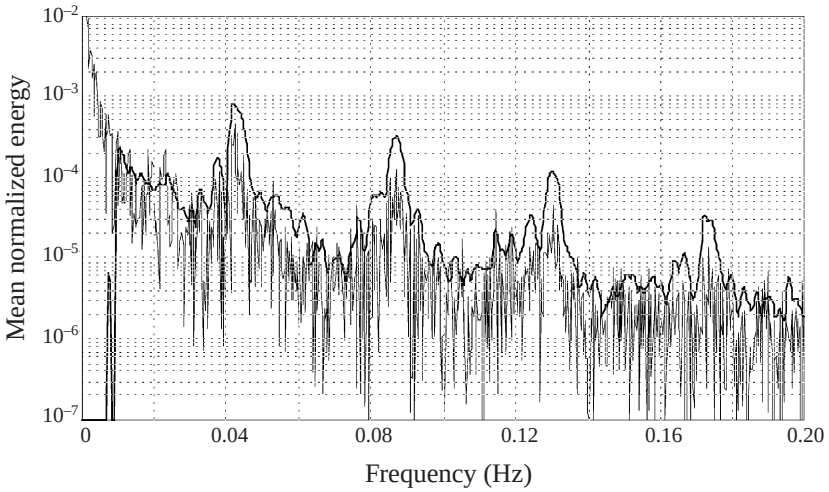

FIGURE 19. Spectral energy density (light line) and its mean value (thick line) slightly shifted. $N = 0.82\,\mathrm{rad\,s^{-1}}$, $\Omega = 2\,\Omega_c$.

first observation in figure 19 is that the noise level is far larger than in the preceding regimes, the frequency peaks being much broader.

A time–frequency analysis of the temporal signal is shown in figure 20. For a periodic signal, we should obtain horizontal straight lines (the fundamental and its harmonics). The phenomena here are clearly more chaotic. Two bubbles of periodicity are observed around $100 < t < 500\,\mathrm{s}$ and $2500 < t < 2800\,\mathrm{s}$. At $t \sim 1000\,\mathrm{s}$ and $2000 < t < 2500\,\mathrm{s}$, no signal is recorded, whereas at $t \sim 1500\,\mathrm{s}$ and $t \sim 3500\,\mathrm{s}$, broad band components are present.

The first broad-band component zone ($t \sim 1500\,\mathrm{s}$) corresponds to the fast decrease of the mean density at the probe location, the amplitude of the fluctuations being constant. The second broad-band zone seems, however, to characterize a weakly

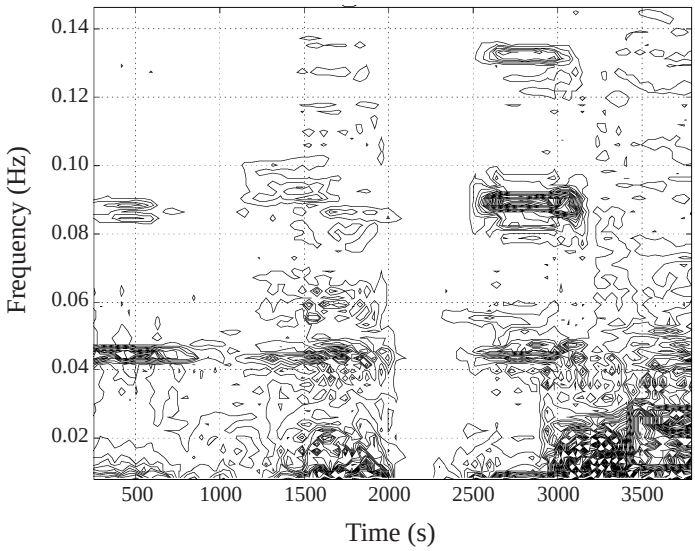

FIGURE 20. Iso-density contours of frequency versus time in the T regime for $N = 0.82\,\mathrm{rad\,s^{-1}}$, $\Omega = 2\,\Omega_c$.

turbulent behaviour at the location of the probe, a behaviour that has also been observed in the visualizations.

Since we are not able to visualize the flow and measure the density fluctuations at the same time (the injection of fluorescein changes the conductivity locally), we cannot directly link the density measurements to the visualizations.

In conclusion, the visualizations indicate a form of weak turbulence which appears at $\epsilon \simeq 0.5$. Recall that, in the homogeneous case, for a large aspect ratio system, weak turbulence appears for $\epsilon \simeq 12$ (Fenstermacher, Swinney & Gollub 1979). For a small aspect ratio system ($\Gamma \simeq 5$), a chaotic regime was also observed close to the threshold by Mullin, Cliffe & Pfister (1987). Theoretical work on magnetoconvection in an infinite system (Rucklidge 1994) suggests that the early appearance of weak turbulence might be the consequence of the existence of a global bifurcation.

4.5. *Regime CT*

4.5.1. *Visualizations*

The last regime we have studied is labelled CT for 'Compact Taylor vortices'. The visualizations presented in figure 21 show that the wavelength of the structures is equal to twice the gap width, with *no* size distribution, as in the homogeneous case. There is also a well-defined temporal sequence where a given cell grows, then exchanges fluid with a neighbouring cell, and then shrinks. Moreover, records of both plane sections of the gap show that the flow is non-axisymmetric. These observations are identical to those of Hua *et al.* (1997*a*) and show striking similarities between the CT regime and the wavy vortices regime in homogeneous Taylor–Couette flow (Wereley & Lueptow 1998). This means that the CT regime is probably a regime of wavy vortices. This would imply non-turbulent spectra for velocity fluctuations. However, because fluid is periodically exchanged between adjacent overturning vortices, there should be chaotic mixing (Solomon, Thomas & Warner 1998). In other words, the flow allows fluid particles of different densities to come near to each other. Hence, density fluctuation spectra should be very noisy.

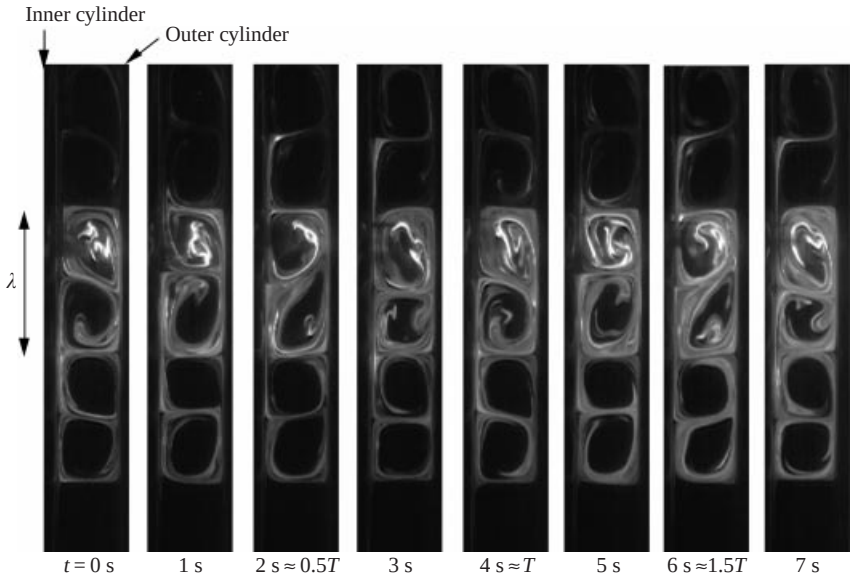

FIGURE 21. Temporal sequence of dye visualizations in the CT regime. $N = 0.88\,\mathrm{rad\,s^{-1}}$, $\Omega = 4\,\Omega_c$.

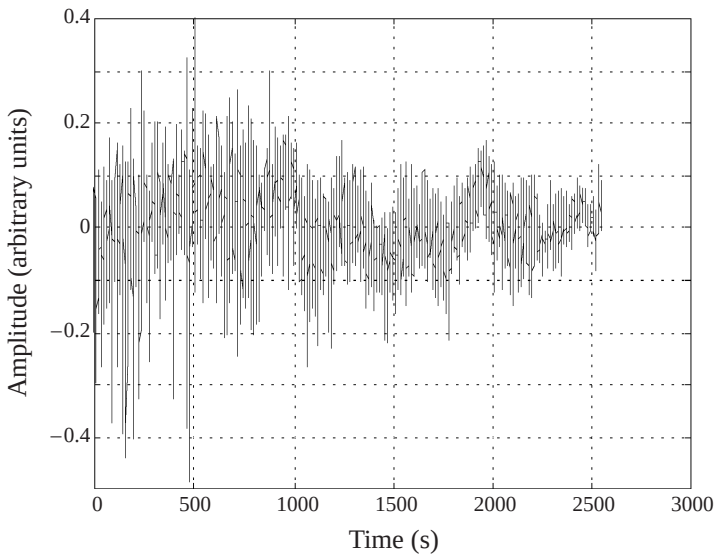

FIGURE 22. Temporal evolution of the density fluctuations in the CT regime. $N = 0.82\,\mathrm{rad\,s^{-1}}$, $\Omega = 5.1\,\Omega_c$.

4.5.2. *Density measurements*

The temporal evolution of the density fluctuations in established flow conditions is presented in figure 22. As expected from the forgoing discussions, the signal looks noisy and its amplitude decreases slowly in time, indicating mixing. Note that as much as 25 min (1500 s) is needed to decrease the amplitude of figure 22 by a factor two. This agrees with the snapshot of figure 5(*c*) of Hua *et al.* (1997*a*) which indicates a step-like density profile, with strong density gradients appearing each wavelength.

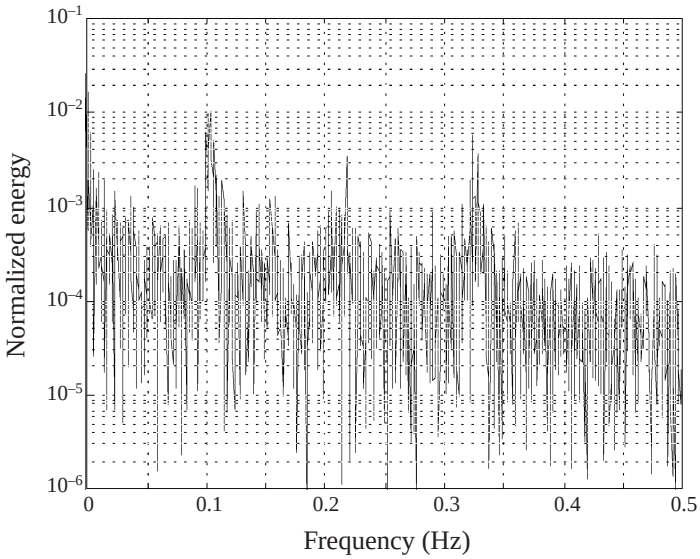

FIGURE 23. Spectral density energy. $N = 0.82\,\mathrm{rad\,s^{-1}}$, $\Omega = 5.1\,\Omega_c$.

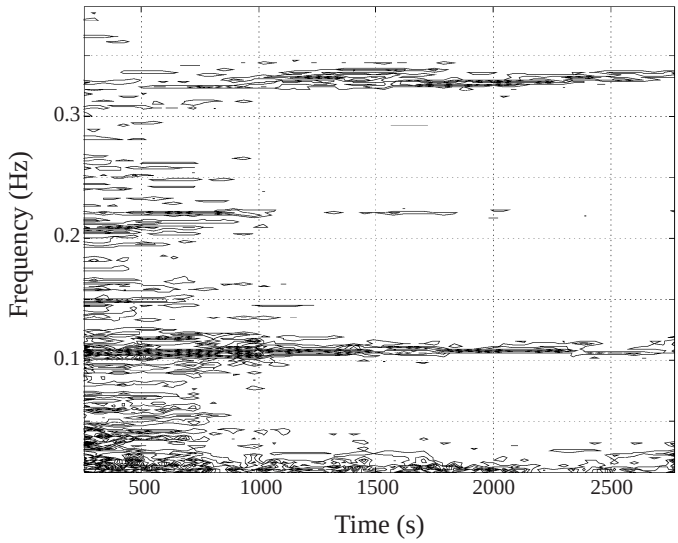

FIGURE 24. Iso-density contours of frequency versus time in CT regime $N = 0.82\,\mathrm{rad\,s^{-1}}$, $\Omega = 5.1\,\Omega_c$.

Within two vortices (one wavelength) density variations are weak, except in the local fluid exchange region.

Figure 23 shows that the spectrum is much more peaked than in the preceding T regime. However, the noise level is still very large compared to the wave or stratified vortex regimes. Cross-correlated spectra confirm that the flow is non-axisymmetric. To give more information about this flow regime, a time-frequency analysis is presented in figure 24. It is seen that the large-band noise present at the beginning of the record decreases in time, a behaviour expected from the temporal record. For $t > 1000\,\mathrm{s}$, the flow is nearly periodic as can be seen from the horizontal lines.

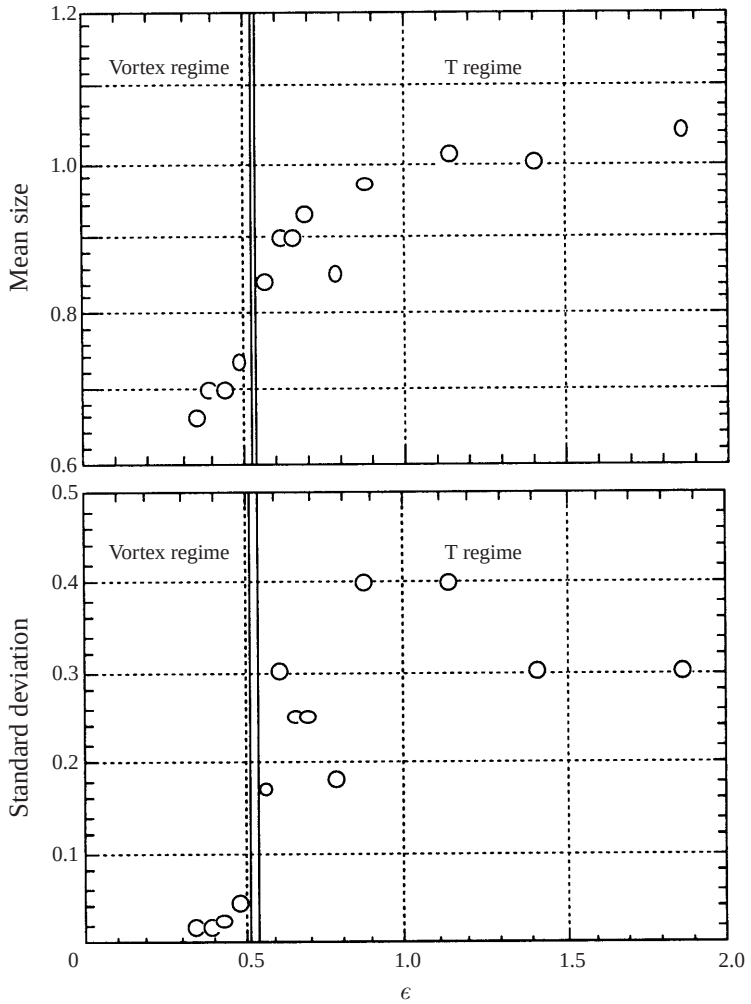

FIGURE 25. Mean value ($\bar{\lambda}/2d$) and standard deviation of the axial structure size versus the distance to threshold (ϵ) for $N = 0.82\,\mathrm{rad\,s^{-1}}$. The mean sizes and standard deviations are non-dimensionalized by the gap width.

We conclude that this regime is a wavy vortices regime. The noise is related with the chaotic mixing, causing the density to be more uniform within a wavelength as time passes. This reappearance of periodic structures, interpreted as wavy vortices as observed in homogeneous Taylor–Couette flow, after a weakly turbulent regime, will be explained by a simple energy argument in § 5.1.

4.6. *Structure size*

Up to this point, the temporal behaviour of the flow has mainly been considered. From the vizualisations it is also possible to determine the axial size distribution of the vortex structures. We calculated the mean non-dimensional structure size ($\bar{\lambda}/2d$) and its standard deviation, over typically 10 cells, for a given stratification. Figure 25 displays a smooth evolution of the mean structure size with the control parameter. There is regular growth until $\epsilon \simeq 0.8$ where the non-dimensioned size saturates at about 1. This is possible in this closed system, because end boundary conditions are

of no importance in stratified flows. The standard deviation has a clear jump at the transition between the stratified vortex and Taylor vortex regimes at $\epsilon \simeq 0.5$. These results are in good agreement with the numerical simulations of Hua *et al.* (1997*a*). The experimental method of Boubnov *et al.* (1995) did not allow this evolution to be determined. Nevertheless, a close look at their figure 6(*b*) shows that, at mid-height of the photograph, structures of aspect ratio $\frac{1}{2}$ are present, whereas much larger structures exist at the bottom. Our main result is that the mean size of the structures increases *continuously* with rotation rate, until it reaches the size of the gap. The second important result is that there is a sudden appearance of size distribution for a rotation rate corresponding to the transition between the stratified vortex and Taylor vortex regimes; this distribution is probably linked to the existence of defects in this T regime.

5. Further discussion and conclusions

5.1. *Energy argument*

Energy considerations allow simple explanations for the observed vortex sizes to be obtained as a function of Ω. We consider here that the inertial and stratification effects are dominant, so that viscosity effects can be neglected. Consider a fluid particle near the inner cylinder, of kinetic energy $E_c = \frac{1}{2}\rho(a\Omega)^2$. This energy can be converted into potential energy $E_p = \rho h^2 N^2$, where h is the height with respect to the original position of the particle and ρ the particle density. The maximum height allowed by the stratification for a cell structure is thus

$$\rho h^2 N^2 \leqslant \tfrac{1}{2}\rho(a\Omega)^2 \rightarrow \frac{h_{max}}{d} \leqslant \frac{a}{\sqrt{2}d}\frac{\Omega}{N}. \tag{5.1}$$

This expression is very similar to the one obtained in the linear stability analysis (3.26), and also to the expression obtained by Boubnov *et al.* (1995). Note that (3.26) is obtained for confined internal waves whereas the expression in Boubnov *et al.*, which is identical except from the numerical factor, is valid for stationary axisymmetric vortices. So the numerical proportionality factor contains the details of the flow.

So, for the wave and stratified vortex regimes the maximum height of the structures is fixed by the stratification, because $h_{max}/d < 1$ in these regimes. When Ω is increased, the maximum height allowed by the stratification approaches the gap width. As a consequence, the structure size begins to be dependent not only on the stratification but also on the radial boundary conditions. Thus, the T regime exhibits a competition between a stratification-dominated flow and an inertia-dominated flow. In this regime stationary vortices of aspect ratio 1 (Taylor vortices) can be present. To get compact Taylor vortices (fluid is exchanged between vortices within a wavelength) the particle must be allowed to make excursions up to $h = 2d$. In this case, the homogeneous flow should nearly be recovered. This qualitative reasoning explains the similarities between the CT regime and wavy vortices in homogeneous fluid and can predict the slope of the threshold between the T and CT regimes. From (5.1) we get

$$\frac{\Omega_{T\rightarrow CT}}{N} = 2\frac{\sqrt{2}d}{a} = 0.84. \tag{5.2}$$

This is in reasonably good agreement (see figure 26) with the experimental data of Boubnov *et al.* (1995).

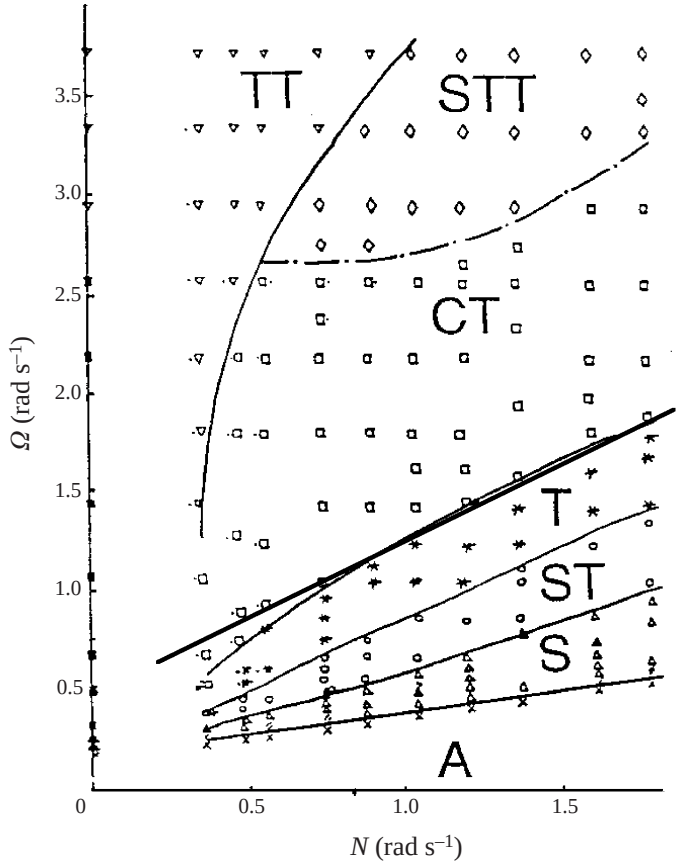

FIGURE 26. Experimental flow regimes diagram from Boubnov *et al.* (1995). The solid straight line (slope 0.84) comes from the energy argument (5.2).

5.2. *Similarities with other flows depending on two control parameters*

In an extended system, a bifurcation diagram similar to the one we observed has only been proposed theoretically for convection subjected to a magnetic field (Rucklidge 1994). Its possible existence has, however, never been demonstrated experimentally or numerically. On the other hand, primary Hopf bifurcations and global bifurcations have been extensively studied in confined systems (Peacock, Binks & Mullin 1999; Delouche 1996; Millour *et al.* 1999), and specifically in small aspect ratio homogeneous Taylor–Couette flow (Mullin *et al.* 1987; Mullin 1993) in which cases the boundary effects are crucial. The diagram shown in figure 14*b* is thought to be generic for extended systems with two independent control parameters with opposite effects, one destabilizing and the other one stabilizing. When the typical disappearance time associated with the stabilizing control parameter is larger than the typical dissipation time of instability, the primary bifurcation must be oscillatory. This criterion gives a critical non-dimensional number (ratio of typical times) equal to one. Several hydrodynamic systems have such control parameters with opposite effects: thermal convection in rotating systems (Chandrasekhar 1961; Thorpe 1966; Knobloch 1997; Zhong, Ecke & Steinberg 1993), convection with magnetic field (Chandrasekhar 1961) and convection in binary fluids with negative separation ratio (Kolodner *et al.* 1986; Schöpf & Zimmermann 1993; Barten *et al.* 1995). This is also the case in magnetic

Stabilizing \ Destabilizing	Convection	Differential rotation
Rotation	Prandtl $\nu/\kappa_T \leqslant 0.67$	$\nu/\nu = 1$ (marginal)
Density gradient	Lewis $\kappa_C/\kappa_T \leqslant 1$[(a)]	Schmidt $\nu/\kappa_C \geqslant 1.44$
Magnetic field	Roberts $\eta/\kappa_T \leqslant 1$	$\nu/\eta \geqslant 1$[(a)]

TABLE 1. Criteria for oscillatory onset of instability for different analogous systems. Stabilizing and destabilizing control parameters are in columns and rows, respectively. Diffusion coefficients: ν = kinematic viscosity, κ_T = thermal diffusivity, κ_C = chemical diffusivity, η = magnetic viscosity. For references see text. [(a)] The value 1 is an estimation, not an analytical result.

Taylor–Couette flow (Chang & Sartory 1967) and as we show, in stably stratified Taylor–Couette flow. The case of contra-rotating Taylor–Couette flow (Andereck *et al.* 1986) is marginal since the typical time scales are equal.

The analytical threshold for an oscillatory instability has been calculated for rotating convection, magnetoconvection (Chandrasekhar 1961), and now in stratified Taylor–Couette (3.22). Note that in the case of magnetoconvection, the above physical argument gives the theoretical value. In table 1 we summarize the criteria for oscillatory onset of instability for all these systems.

In all these systems, when the oscillatory onset of instability is satisfied, one should expect a global bifurcation as the secondary bifurcation. Indeed, if stationary non-axisymmetric structures are stable, they cannot connect to the oscillatory state through a local bifurcation. The existence of a global bifurcation in these systems should also lead to an early appearance of weak turbulence as pointed out by Rucklidge (1994) and Mullin (1993), and observed in our system.

5.3. *Conclusion*

We provide in this paper the first experimental evidence of the existence of a novel bifurcation scenario in hydrodynamics for an extended system. Adding an independent stabilizing control parameter (stable density stratification) to the well-known Taylor–Couette flow with only the inner cylinder rotating (unstable stratification of angular momentum) changes radically the route to chaos. The primary bifurcation does not lead to a stationary structure as in homogeneous Taylor–Couette flow when only the inner cylinder is rotating. The axially stratified Taylor–Couette flow bifurcates from the purely azimuthal flow through a direct Hopf bifurcation to an axisymmetric wave regime. Measured values for the critical rotation rate and the critical oscillation frequency of the waves are in very good agreement with the predictions of the linear stability analysis. The next transition, which takes the system into a state of non-axisymmetric drifting vortices, shows hysteresis. From the characteristics of these two states, we propose a bifurcation diagram which reconciles the previous results obtained for the same stratified Taylor–Couette system. It presents a saddle-node global bifurcation and could qualitatively hold for a large class of hydrodynamic systems. The next regime (T) exhibits both stationary structures (similar to Taylor vortices in homogeneous Taylor–Couette flows) and weakly turbulent structures, called sporadic defects. The characterization of this weak turbulence needs the simultaneous acquisition of temporal density fluctuations and flow visualizations at the location of the probe, in order to relate the time–frequency analysis precisely to the 'life' and behaviour of such a defect. The features of the last regime studied in this article (CT) show striking similarities with the wavy vortices regime observed in homogeneous

Taylor–Couette flow. An energy argument is finally derived which gives some insight into the physical reasons for the succession of the regimes for a given stratification.

We acknowledge fruitful discussions with Jean-Marc Chomaz, Vincent Croquette, Olivier Dauchot, Jan-Bert Flor, Bach Lien Hua, Paul Manneville, Chantal Staquet, Laurette Tuckerman and the technical assistance of Serge Layat. This work has been supported by the Centre National de la Recherche Scientifique (GDR-Mécanique des Fluides Géophysiques et Astrophysiques 1074). Our friend and colleague Boris Boubnov died during the writing process of this article and we wish to acknowledge the inspiring impact of his work.

REFERENCES

Andereck, C. N., Liu, S. S. & Swinney, H. L. 1986 Flow regimes in a circular Couette system with independently rotating cylinders. *J. Fluid Mech.* **164**, 155–183.

Ashwin, P. & Rucklidge, A. M. 1998 Cycling chaos: its creation, persistence and loss of stability in a model of nonlinear magnetoconvection. *Physica* D **122** 134–154.

Barten, W., Lücke, M., Kamps, M. & Schmitz, R. 1995 Convection in binary fluid mixtures. I. Extended traveling-wave and stationary states. *Phys. Rev.* E **51**, 5636–5670.

Billant, P. & Chomaz, J. M. 2000 Experimental evidence for a new instability of a vertical columnar vortex pair in a strongly stratified fluid. *J. Fluid Mech.* **418**, 167–188.

Bottin, S., Dauchot, O., Daviaud, F. & Manneville, P. 1998 Intermittency in a locally forced plane Couette flow. *Phys. Fluids* **10**, 2597–2607.

Boubnov, B. M., Gledzer, E. B. & Hopfinger, E. J. 1995 Stratified circular Couette flow: instability and flow regimes. *J. Fluid Mech.* **292**, 333–358.

Boubnov, B. M. & Hopfinger, E. J. 1997 Experimental study of circular Couette flow in a stratified flow. *Fluid Dyn.* **32**, 520–528.

Busse, F. H. & Clever, R. M. 1996 Higher bifurcations in fluid flows and coherent structures in the turbulent state. *Advances in Turbulence VI* (ed. S. Gavrilakis *et al.*), pp. 309–312. Kluwer.

Caton, F. 1998 Ecoulement de Taylor–Couette stratifié: Régimes, bifurcations et transport. Thèse de doctorat, Universite Joseph Fourier, Grenoble.

Caton, F., Janiaud, B. & Hopfinger, E. J. 1999 Primary and secondary Hopf bifurcations in stratified Taylor–Couette flow. *Phys. Rev. Lett.* **82**, 4647–4650.

Chandrasekhar, S. 1961 *Hydrodynamic and Hydromagnetic Stability*. Dover.

Chang, T. S. & Sartory, W. K. 1967 On the onset of instability by oscillatory modes in hydromagnetic Couette flow. *Proc. R. Soc. Lond.* A **301**, 451.

Couette, M. 1890 Etude sur le frottement liquide. *Ann. Chim. Phys.* **21**, 433.

Cross, M. C. & Hohenberg, P. C. 1993 Pattern formation outside of equilibrium. *Rev. Mod. Phys.* **65**, 851–1009.

Dauchot, O. & Manneville, P. 1997 Local versus global concepts in hydrodynamic stability theory. *J. Phys.* II *Paris* **7**, 371–389.

Delouche, E. 1996 Convection thermosolutale avec effet Soret en milieu confiné. Thèse de doctorat, Universite Paris-Sud.

Delouche, E., Labrosse, G. & Tric, E. 1996 The oscillatory 2D convective states of a binary fluid confined in small cavity *J. Phys.* III *Paris* **6**, 1527–1534.

Di Prima, R. C. & Swinney L. H. 1981 Instabilities and transition in flow between concentric rotating cylinders. In *Topics in Applied Physics, Hydrodynamic Instability and the Transition to Turbulence* (ed. R. C. Di Prima, L. H. Swinney & J. P. Gollub). Springer.

Fenstermacher, P. R., Swinney, H. L. & Gollub, J. P. 1979 Dynamical instabilities and the transition to chaotic Taylor vortex flow. *J. Fluid Mech.* **94**, 103–128.

Gollub, J. P. & Freilich, M. H. 1976 Optical heterodyne test of perturbation expansions for the Taylor instability. *Phys. Fluids* **19**, 618–626.

Guckenheimer, J. & Holmes, P. 1983 *Non-linear Oscillations, Dynamical Systems and Bifurcations of Vector Fields*. Springer.

Handbook of Chemistry and Physics 1996 D. P. Lide, Editor in Chief 76 Edition. CRC Press.

Hua, B. L., Le Gentil, S. & Orlandi, P. 1997*a* First transitions in circular Couette flow with axial stratification. *Phys. Fluids* **9**, 365–375.

Hua, B. L., Moore, D. W. & Le Gentil, S. 1997*b* Inertial non-linear equilibration of equatorial flows. *J. Fluid Mech.* **331**, 345–371.

Knobloch, E. 1997 Symmetry and instability in rotating hydrodynamic and magnetohydrodynamic flows. *Phys. Fluids* **8**, 1446–1454.

Kolodner, P., Passner, A., Surko, C. M. & Walden, R. W. 1986 Onset of oscillatory convection in a binary fluid mixture. *Phys. Rev. Lett.* **56**, 2621–2624.

Manneville, P. 1991 *Dissipative Structures and Weak Turbulence*. Collection Alea Saclay, Gif-sur-Yvette, France (also Cambridge University Press 1991).

Millour, E., Delouche, E., Tric, E. & Labrosse, G. 1999 Subcritical transition to quasi-traveling waves in binary fluid convection confined in a cylindrical container. *Entropie* **218**, 30–35.

Mullin, T. 1993 *The Nature of Chaos*, pp. 74–93. Oxford University Press.

Mullin, T., Cliffe, K. A. & Pfister, G. 1987 Unusual time-dependent phenomena in Taylor–Couette flow at moderately low Reynolds number. *Phys. Rev. Lett.* **58**, 2212–2215.

Nicolaou, D., Liu, R. & Stevenson, T. N. 1993 The evolution of thermocline waves from an oscillatory disturbance. *J. Fluid Mech.* **254**, 401–416.

Oster, G. 1965 Density gradients. *Sci. Am.* **213**, 70–76.

Park, Y. G, Whitehead, J. A. & Gnanadeskian, A. 1994 Turbulent mixing in stratified fluids: layer formation and energetics. *J. Fluid Mech.* **279**, 279–311.

Peacock, T., Binks, D. J. & Mullin, T. 1999 From low- to high-dimensional dynamics in a microscopic fluid flow. *Phys. Rev. Lett.* **82**, 1446–1449.

Rhines, P. B. & Young, W. R. 1983 How rapidly is a passive scalar mixing within closed streamlines? *J. Fluid Mech.* **133**, 133–145.

Rucklidge, A. M .1994 Chaos in magnetoconvection. *Nonlinearity* **7**, 1565–1591.

Schöpf, W. & Zimmermann, W. 1993 Convection in binary fluids: Amplitude equations, codimension-2 bifurcation, and thermal fluctuations. *Phys. Rev.* E **47**, 1739–1764.

Solomon, T. H., Thomas, S. & Warner, J. L. 1998 Chaotic mixing of immiscible impurities in a two-dimensional flow. *Phys. Fluids* **10**, 342–350.

Taylor, G. I. 1923 Stability of a viscous liquid contained between two rotating cylinders. *Phil. Trans. R. Soc. Lond.* A **223**, 289–343.

Thorpe, S. A. 1966 The stability of stratified Couette flow. *Notes on 1966 Summer study program in Geophysical Fluid Dynamics at the Woods Hole Oceanographic Inst.* (WHOI, Woods Hole, 1966), pp. 80.

Wereley, S. T. & Lueptow, R. M. 1998 Spatio-temporal character of non-wavy and wavy Taylor–Couette flow. *J. Fluid Mech.* **364**, 59–80.

Withjack, E. M. & Chen, C. F. 1974 An experimental study of Couette instability of stratified fluids. *J. Fluid Mech.* **66**, 725–737.

Zhong, F. Ecke, R. E. & Steinberg, V. 1993 Rotating Rayleigh-Bénard convection: asymmetric modes and vortex states. *J. Fluid Mech.* **249**, 135–159.